Conduit dynamics of the Rungwe Pumice eruption (Tanzania): From storage to fragmentation of phonolitic-trachytic magmas

Lorenzo Cappelli – *Department of Geosciences, Environment and Society; Université libre de Bruxelles; Bruxelles, 1050, Belgium.* lorenzo.cappelli@ulb.be

Gianmarco Buono – *Istituto Nazionale di Geofisica e Vulcanologia; Italy.* gianmarco.buono@ingv.it

Lucia Pappalardo – *Istituto Nazionale di Geofisica e Vulcanologia; Italy.* lucia.pappalardo@ingv.it

Thomas D. van Gerve – *Department of Earth and Environmental sciences, KU Leuven, Leuven, Belgium.* thomas.vangerve@kuleuven.be

Olivier Namur – *Department of Earth and Environmental sciences, KU Leuven, Leuven, Belgium.* olivier.namur@kuleuven.be

Vanessa N. Sielenou - *Department of Geosciences, Environment and Society; Université libre de Bruxelles; Bruxelles, 1050, Belgium.* vanessa.nguemo.sielenou@ulb.be

Gerald G.J. Ernst – *no affiliation.* plumeman2000@yahoo.co.uk

Evelyne Mbede – *School of Mines and Geosciences; University of Dar es Salaam; Dar es Salaam, 35052, Tanzania.* embede@gmail.com

Shimba Kwelwa – *AngloGold Ashanti; Geita, 532, Tanzania.* skwelwa750@gmail.com

Edista Abdallah – *School of Mines and Geosciences; University of Dar es Salaam; Dar es Salaam, 35052, Tanzania.* edisteralex@gmail.com

Karen Fontijn - *Department of Geosciences, Environment and Society; Université libre de Bruxelles; Bruxelles, 1050, Belgium.* karen.fontijn@ulb.be

Keywords: East African Rift; Peralkaline magmas explosivity; 3DμXCT; Conduit dynamics; Magma fragmentation.

This manuscript is a non-peer-reviewed preprint submitted to EarthArXiv

Abstract

The eruptive style and explosivity of a rising magma are initially shaped by the conditions established in the magmatic plumbing system. However, processes in the conduit during ascent exert a large influence on the final eruption style. Peralkaline magmas—bearing an agpaitic index>1—typically have high water saturation levels, promoting explosive behaviour during ascent. At the same time, their relatively low viscosities—resulting from alkaline-induced Si-O bonds depolymerisation—suggest higher pressure thresholds for bubble bursting or the capacity to endure prolonged plastic deformation under intense stretching stresses. This implies an increased resistance to fragmentation compared to high-silica, calc-alkaline magmas. Yet, trachytic or phonolitic magmas can still produce highly explosive eruptions as confirmed by many documented events. The Rungwe Pumice eruption (Tanzania) serves as a striking example of unexpected eruptive behaviour. This Plinian, VEI 5 eruption was generated by a crystal-poor, microlite-free phonolitic/trachytic magma stored at high temperatures and relatively low water concentrations. Based on these characteristics, a milder eruption might have been expected. However, through detailed 2D and 3D textural analyses of pumiceous ash clasts, we identified a delayed homogeneous bubble nucleation event (ΔP_{sat}~50 MPa) occurring abruptly at shallow depths (Pn~40 MPa). The rapid nucleation and growth of bubbles during fast magma ascent (~6 $MPa \cdot s^{-1}$) left insufficient time to form a highly vesicular foam (ϕ<75%), while low magma permeability hindered efficient outgassing. This maintained a strong coupling between magma and gases, and, combined with a sudden rheological shift likely triggered by volatile loss and a temperature drop, ultimately led to fragmentation and the explosive nature of the eruption. The Rungwe Pumice eruption highlights the critical role of conduit dynamics in shaping the behaviour of peralkaline magmas, which can unexpectedly deviate from predictions based solely on their composition and storage conditions.

1. Introduction

Plinian-style explosive eruptions rank among the most severe natural hazards, with impacts ranging from local to regional and even global scales (e.g., Carey and Sigurdsson, 1989; Cioni et al., 2015). These eruptions are governed by a combination of pre-eruptive magmatic conditions—particularly water concentrations and melt composition (e.g., Wilson et al., 1980; Cioni, 2000)—and the dynamic processes occurring within the conduit during magma ascent. Pre-eruptive factors, such as volatile saturation, magma storage depth, and temperature, set the stage for eruption potential by controlling bubble nucleation, crystallisation, and magma rheology (Cashman and Mangan, 1994; Dingwell, 1996; Gonnermann and Manga, 2007; Cassidy et al., 2018). However, it is within the conduit that magma undergoes a dramatic transformation—from a hot, pressurized silicate melt to a high-energy bubble suspension capable of sustaining explosive fragmentation (Sparks, 1978; Wilson et al., 1980; Cashman and Mangan, 1994). This transformation is driven by rapid decompression, bubble nucleation, and bubble growth, which induce intense shear stress and strain within the magma, ultimately leading to fragmentation (e.g., Dingwell, 1996; Zhang, 1999).

Understanding the conduit dynamics that dictate the transition between effusive and explosive eruptive style is crucial for predicting eruption explosivity and associated hazards. These dynamics have been extensively studied across a variety of magmatic compositions. For fast-ascending, highly viscous silicic magmas, homogeneous nucleation under high supersaturation conditions is commonly inferred (e.g., Shea 2017 and references therein), which eventually leads to strain rate-induced brittle failure (Gonnermann, 2015 and references therein). In contrast, for less-viscous, basaltic magmas, heterogeneous nucleation, abrupt rheological changes, or external perturbations (e.g., magma-water interactions) have been suggested to govern eruptive explosivity (e.g., Giordano and Dingwell, 2003; Houghton and Gonnermann, 2008), with ascent rate having a dominant control on preventing outgassing despite high bubble connectivity and permeability (e.g., Houghton et al., 2004; Burgisser et al., 2017; Bamber et al., 2024). Peralkaline felsic magmas possess complex physicochemical properties (Polacci et al., 2004; Shea et al., 2017) but are known to feed explosive eruptions (e.g., Pappalardo and Mastrolorenzo, 2012; Hughes et al., 2017; Shea et al., 2017; Pappalardo et al., 2018; Stabile et al., 2021; Wallace et al., 2025). With relatively elevated silica concentrations ($SiO_2 \geq 60$ wt.%) and significant water content (up to 8 wt.% at 200 MPa; e.g., Carroll and Blank, 1997; Di Matteo et al., 2004), these magmas ascend rapidly within the conduit through density-driven isostatic processes (Browne and Szramek, 2015), undergoing dramatic acceleration as bubbles form and expand. Moreover, alkali-induced depolymerisation lowers melt viscosity (Di Genova et al., 2013), reducing frictional resistance along conduit walls and potentially resulting in ascent rates higher than those of calc-alkaline magmas. However, since such moderately low viscosity typically drives effusive or weakly explosive eruptions, investigating the eruptive dynamics behind highly explosive events fed by these magmas remains of relevant interest.

This study focuses on conduit processes, highlighting their role in shaping the eruptive behaviour of the Rungwe Pumice (RP) eruption and providing insights into the mechanics of sustained explosive activity of phonolitic-trachytic magmas. The RP eruption offers a unique opportunity to explore the interplay between magmatic dynamics and eruptive processes. We employ an integrated approach combining traditional 2D textural analysis methods (Cashman and Mangan, 1994; Shea et al., 2010; Gurioli et al., 2015) with advanced 3D imaging techniques using X-ray microcomputed tomography (μXCT; Polacci et al., 2010; Giachetti et al., 2011; Hughes et al., 2017; Pappalardo et al., 2018, 2023; Valdivia et al., 2022; Buono et al., 2023). While 2D imaging methods provide valuable insights into vesicle characteristics, they are limited in their ability to represent real textural features and require stereological corrections (Shea et al., 2010). Moreover, 2D analyses cannot fully resolve permeability or vesicle network connectivity (Giachetti et al., 2011). In contrast, μXCT allows for direct, non-destructive 3D observations of these features. However, μXCT accessibility restricts the number of analysed samples and may limit representativity. In complement to these analyses, we utilised embayment water diffusion speedometry (Liu et al., 2007) to validate ascent rates estimated from textural data. By combining these techniques, this study aims to provide a comprehensive understanding of the conduit dynamics that sustained the explosive activity of peralkaline phonolitic-trachytic magma during the RP eruption.

2. Geological Background

The East African Rift (EAR) is generated by the divergence of the Somalian and Nubian (African) Plates and extends over 3000 km southward from the Afar triple junction to Mozambique (Saria et al., 2014). In its central part, the rift encounters the thick and rigid Tanzanian craton, splitting into two sectors known as Western and Eastern branches (Saria et al., 2014; Ebinger et al., 2017). Volcanism is widespread along the EAR, producing magmatic compositions spanning from mafic to silicic, with a notable prevalence of high alkali concentrations (e.g., Macdonald and Scaillet, 2006; Hutchison et al., 2018).

The Rungwe Volcanic Province (RVP), covering over 1500 km^2, is located in the Western branch of the EAR, south of the Tanzanian Craton at the junction of the NW-SE trending Tanganyika-Rukwa rift, the N-S trending North Malawi rift and the NE-SW trending Usangu basin (**Fig. 1a;** Ebinger et al., 1993). The RVP comprises three main Holocene volcanic centres—Rungwe, Ngozi and Kyejo—surrounded by several smaller eruptive centres, distributed along two dominant NW-SE and NE-SW alignments (Harkin, 1960; Fontijn et al., 2010a). Volcanic activity in the RVP began approximately 9 Ma, alternating between effusive and explosive eruptions of high-alkali magmas (Fontijn et al., 2010b, 2012). During the late Quaternary, the region has been predominantly marked by explosive events, including Plinian-style eruptions, with sparse occurrences of effusive volcanism (Fontijn et al., 2010b, 2012 and references therein).

Rungwe, the largest volcanic edifice in the RVP, is a relatively young stratovolcano (0.25 ±0.01 Ma, whole-rock K-Ar age on a lava flow at the base of the edifice; Ebinger et al., 1989) centrally located in the province (**Fig. 1b**). It predominantly produced magmas of basaltic, phonolitic, and trachytic compositions. Over its history, Rungwe is estimated to have experienced at least one explosive eruption every 500 years, ranging from violent Strombolian to Plinian events (Fontijn et al., 2010b). Among these, the Rungwe Pumice Plinian eruption stands out as the largest event in the province's Holocene history (Fontijn et al., 2011).

2.1. Rungwe Pumice Eruption

The RP deposit consists of a massive pumice lapilli fall deposit that blankets the entire RVP. Radiocarbon dating and sedimentary records from Lake Masoko place the eruption at ~4 ka cal BP (Garcin et al., 2006; Fontijn et al., 2010b). The deposit is lithic-poor and predominantly consists of cream-coloured, highly vesiculated pumice lapilli of high-alkaline, trachytic composition (whole-rock; Fontijn et al., 2013). A minor component (<1wt%) of grey/banded pumice was found and interpreted as evidence of mingling with a slightly more mafic magma (Fontijn et al., 2011). Alkali feldspar is the primary free mineralogical component, followed by subordinate amounts of biotite, clinopyroxene and Fe-Ti oxides. Notably, cyan-coloured haüyne occurs in the RP deposit, distinguishing it from most other RVP deposits and serving as a field marker for identifying RP outcrops (Fontijn et al., 2011).

More than 100 RP outcrops were mapped across the province extending up to 28 km from Rungwe summit, where the deposit maintains a thickness of 30 cm. A ~1 m-thick tephra layer attributed to the RP eruption was found in Lake Masoko's sedimentary record around 25 km

SSE of Rungwe (Garcin et al., 2006; Fontijn et al., 2012). More distal deposits are absent and have likely undergone pedogenesis. However, sediment cores from Lake Malawi, drilled ~115 km SE of Rungwe, contain visible ash horizons chronologically correlated with the RP eruption (Fontijn et al., 2011).

RP outcrops are radially distributed around the summit, with near-circular isopleths indicating that the eruption originated from the current Rungwe summit and likely occurred under wind-still conditions, though the exact vent location remains poorly constrained (Fontijn et al., 2011). A peak eruptive column height of 30-35 km was inferred using the maximum lithics method (Carey and Sparks, 1986; Fontijn et al., 2011), which was likely sustained throughout most of the eruption, as no associated pyroclastic density current deposits were found. The peak mass discharge rate, calculated using a range of inferred column heights, ranges from 2.8 to 6.0 $\times 10^8$ $kg \cdot s^{-1}$, and the minimum erupted volume is estimated at 1.4 km^3 dense rock equivalent (Fontijn et al., 2011). Based on these parameters, the eruption is classified as Plinian, with a Volcanic Explosivity Index of 5 (Newhall and Self, 1982; Fontijn et al., 2011).

A type section for RP deposit was identified ~11.7 km SSE of the Rungwe summit and designated as KF176 in previous studies (**Fig. 1b**; Fontijn et al., 2010b, 2011, 2013). The section comprises a ~2.5 m-thick, massive pumice deposit reversely graded at the base and bounded by overlying and underlying palaeosols. The deposit was previously sampled through its entire thickness by Fontijn et al. (2011) and subdivided into 14 samples every 20-25 cm from base to top and labelled sequentially from KF176-B to KF176-O, whereas KF176-A corresponds to the basal palaeosol.

The RP plumbing system has been described as a relatively hot reservoir—ranging from 925 to 975 ±22 °C (Fontijn et al., 2013; Cappelli et al., 2025)—of trachytic-phonolitic composition (haüyne-hosted melt inclusions major element concentrations). Prior to the eruption, it ponded at shallow crustal depths (~3.5 km, minimum depth based on saturation pressure models derived from haüyne-hosted melt inclusions; Cappelli et al., 2025) and yielded on average ~4.82 ±0.58 wt.% of dissolved water while CO_2 resulted below FTIR detection limit (< 10-100 ppm; Cappelli et al., 2025). The system was likely destabilised by an input of volatile-rich magma, which increased oxygen fugacity, ultimately leading to the eruption (Fontijn et al., 2013; Cappelli et al., 2025).

3. Methods

Samples from the Rungwe Pumice eruption type section KF176 were dry-sieved down to 63 µm and subdivided into granulometric size classes at φ/2 intervals (φ = $-\log_2$[*diameter*(mm)]). For ease of data interpretation, samples were grouped into five stratigraphic horizons: base (KF176 C-D), bottom half (KF176 E-F-G), middle (KF176 H-I-J), top half (KF176 K-L-M), and top (KF176 N-O). Subsequent analyses kept this partitioning scheme and targeted specific samples as representative of each horizon.

3.1. Embayment diffusivity speedometer

Magma decompression rates were estimated based on the decompression-induced, diffusivity-dependent decrease in volatile concentrations within crystal-hosted melt (glass) embayments. Volatile concentration tends to decrease from the innermost portions of embayments to their outlets, which remain in contact with the external melt and undergo re-equilibration of volatile saturation during ascent (e.g., Liu et al., 2007; deGraffenried and Shea, 2021; Geshi et al., 2021; Hosseini et al., 2023).

Accurate inspection of glass embayments was conducted in haüyne crystals, the mineralogical phase hosting the largest number and most well-developed melt inclusions among all crystals from the RP eruption (Cappelli et al., 2025). Glass embayments that best preserve volatile concentration gradients tend to exhibit a cylindrical shape, with minimal necking near the outlet and no significant irregularities (deGraffenried and Shea, 2021; Hosseini et al., 2023). They should also be free of decompression bubbles in their internal regions while maintaining contact with an external bubble (or its remnant shape) at the outlet (Hosseini et al., 2023). Approximately 25 crystals, handpicked from crushed pumices, were initially selected for measurement. These were collected from the bottom half, middle, top half and top stratigraphic horizons of RP deposit. Suitable embayments could not be retrieved from the base of the deposit due to the scarcity of haüyne crystals in this stratigraphic portion.

The crystals were individually embedded in Crystalbond™ thermosetting resin and ground to expose the embayment(s). Afterwards, the resin was melted, and crystals were cast all together in an epoxy resin mount and mechanically polished using diamond pastes down to 1µm. Water in embayments' glass was analysed with Raman spectroscopy using a Horiba Jobin LabRAM HR Evolution at KU Leuven (Belgium). Samples were irradiated with an Nd-YAG-sourced laser, maintaining low laser power (≤ 50%) to prevent overheating of the resin—particularly in thin embayments—and to avoid potential damage to the crystals. Scattering spectra were acquired in the 150-4000 cm^{-1} wavenumber range and the SilicH2O open-source software (Van Gerve and Namur, 2023) was used to perform the baseline correction and to extract the peak areas. To account for potential interference in cases where embayments were too thin, and noise from underlying phases was recorded, spectra of the host crystal and pristine resin were also acquired and used to correct the glass spectra (Van Gerve and Namur, 2023). Then, water concentrations in the glass were quantified using the calibration feature of SilicH2O. A calibration curve was constructed by correlating the areas of the silica peaks (200–600 cm^{-1} and 800–1300 cm^{-1} ranges) with the area of the water vibrational peak (~3500 cm^{-1}). This calibration was based on spectra of melt inclusions previously analysed by FTIR spectroscopy, for which water contents were independently determined (Cappelli et al., 2025). Ultimately, only 9 glass embayments across the entire deposit were successfully measured

An embayment speedometer was developed by Liu et al. (2007) and subsequently elaborated by several authors using different input parameters and coding languages. In this study, we adopted the publicly available EMBER software, written in MATLAB (Georgeais et al., 2021). EMBER estimates decompression rates by comparing modelled volatile diffusion profiles with the measured concentration gradients in embayments, thereby determining the best fit for decompression rates, initial dissolved concentrations, and initial exsolved gas content. It can determine decompression rates from H_2O, CO_2 and S concentration gradients, however, in our case only water concentrations were available and therefore other volatiles were excluded. Notably, RP glass—both in haüyne-hosted melt inclusions and embayments—was depleted in CO_2, falling below the FTIR detection limit, indicating a minimal effect on water solubility (Cappelli et al., 2025). Input parameters include: i) temperature, assumed constant throughout the ascent and equivalent to RP storage temperature, previously estimated at 975 ˚C on average (Cappelli et al., 2025); ii) initial pressure, equivalent to RP storage pressure, estimated at 92 ±15 MPa on average based on melt inclusion water content at saturation (Cappelli et al., 2025); and iii) the final pressure before melt quenching, which was iteratively varied between 0.5 and 25 MPa to achieve the best correlation (minimum least error). Degassing paths provided as inputs for EMBER were calculated for seven initial exsolved gas contents (between 0 and 3.2 wt.%; see also Georgeais et al., 2021) under closed-system conditions using VESIcal v1.2.6. (Iacovino et al., 2021) and Thermoengine (Ghiorso and Gualda, 2015) Python libraries, both accessible on ENKI servers. A wide range of exsolved gas contents was considered to evaluate any relevant effect on interpolations as in Georgeais et al. (2021), however, as suggested by melt inclusion analyses (Cappelli et al., 2025), a 0 wt.% initial gas was preferred.

Water diffusivity in EMBER is calculated with three different models according to glass composition: basaltic, rhyolitic and intermediate (Georgeais et al., 2021). For RP composition we applied the diffusivity model for intermediate compositions using the equations from Ni and Zhang (2018), which are tested for calc-alkaline compositions. We acknowledge that this assumption inevitably introduces some uncertainty; however, diffusivity values calculated under identical conditions using equations more appropriate for trachytic (Fanara et al., 2013) or phonolitic compositions (Fanara et al., 2013; Schmidt et al., 2013) produced results of the same order of magnitude (10^{-10} $m^2 \cdot s^{-1}$). To our knowledge, no published embayment speedometer specifically tested for (per)alkaline magmas currently exists. Decompression rates estimated with EMBER were however validated with textural methods (see §3.5).

Silica content (wt.%)—and other major element concentrations—in embayment glasses were measured using a Tescan Mira 4 FEG scanning electron microscope equipped with an Oxford Xplore30 EDX detector at the KU Leuven Core Facility (Belgium). Samples were carbon-coated to a precise thickness of 10 nm, and analysed using an acceleration voltage of 20 keV and a beam current of 6 nA. The Beam Measurement calibration routine integrated into the Oxford Aztec software was used to calibrate Mn elemental concentrations on standard material, ensuring accurate absolute concentrations of major elements. Measurements were performed over areas rather than single spots to minimise the loss of alkali elements, and each embayment was measured 3-10 times to ensure consistency and account for potential variations in glass composition near the embayment outlet. Measurement accuracy was validated by analysing the ATHO-G, StHs6/80-G, and T1-G glass standards (Jochum et al., 2006) multiple times at the start and end of the analytical session. Additionally, glasses of RP crystal-hosted melt inclusions previously analysed with electron probe microanalysis (Cappelli et al., 2025) were used as reference material. For silica concentrations, standards and reference materials yielded a maximum percentage difference to expected values of 0.7% and 0.3% respectively, with a relative standard deviation between measurements of no more than 0.9% (**Supplementary materials**).

3.2. 2D pumice textures

Textures of RP pumice were first evaluated on 2D images of polished sections. Ash particles within the 0/-0.5 φ (1-1.4mm) grain size range from each horizon were rinsed in an ultrasonic bath and then embedded in epoxy resin. A fine grain size range minimises the potential effect of post-fragmentation inflation of gas bubbles that could alter original vesicularity in slower-cooling, larger clasts (Kaminski and Jaupart, 1997; Pappalardo et al., 2018). Moreover, isolated voids in coarser samples often prove difficult to fully impregnate with resin, complicating image processing (Shea et al., 2010). For comparison, coarse pumice lapilli vesicularity was also investigated by combined gas and water displacement pycnometery (based on Archimedes's principle; methodology and results are presented in **Supplementary Material**). Particles were grounded until they were sliced to about half their original volume, then polished with diamond pastes down to 1 μm and finally carbon-coated. Images were acquired in backscattered electron mode (BSE) using an SEC SNE-4500M Plus B scanning electronic microscope equipped with a Bruker EDS Quantax detector at the Laboratoire G-Time of the Université libre de Bruxelles (Belgium). Measurements were performed at an accelerating voltage of 15 keV. For each stratigraphic horizon, one BSE image at x350 magnification was captured for ten randomly selected particles, resulting in a total of 50 analysed particles. The x350 magnification was chosen according to the range of vesicle dimensions (Shea et al., 2010).

Greyscale BSE images were processed using the open-source software Fiji (ImageJ; Schindelin et al., 2012). A preliminary manual rectification was conducted on images to account for vesicles not filled with resin. The Trainable Weka Segmentation tool (Arganda-Carreras et al., 2017) was then applied to classify pumice glass, vesicles and, when present, phenocrysts, producing binary images. Finally, the distance transform watershed algorithm provided in the MorphoLibJ library (Legland et al., 2016) was used to reconstruct vesicle walls lost during sample preparation or due to bubble coalescence during final stage of magmatic ascent.

From the processed binary images, 2D vesicularity (percentage of the area occupied by vesicles), the number of vesicles per unit area (N_a), and the average bubble area were calculated. Each clast was then scored based on the root-sum-of-squares of the variances of these parameters relative to the average value calculated for clasts within the same stratigraphic horizon (i.e., Euclidean distance). The clast bearing the minimum score, representing the least deviation from the average, was identified as the most representative of its stratigraphic horizon and selected for further investigation.

Additional BSE images were collected for these five selected clasts at varying magnifications following the nested image strategy proposed by Shea et al. (2010) for stereological conversion.

Specifically, one image was acquired at a magnification sufficient to capture the entire clast (x67-x100), then two images at x350 were taken from areas exhibiting the greatest vesiculation difference based on visual inspection. Within these areas, two images each were captured at x900 (**Fig. 2**). Images were processed in Fiji as previously described. Using FOAM software (Shea et al., 2010), we then obtained statistical descriptors of shapes and sizes of vesicles corrected for cut-effect and intersection probability (Cashman and Mangan, 1994; Shea et al., 2010 and references therein). Stereological conversion in FOAM utilises vesicularity values constrained by three-dimensional reconstructions of particles (§3.3 and 3.4), as vesicularity estimates from the stereological conversion are prone to overestimation (Shea et al., 2010).

3.3. 3D pumice textures

3D maps of pumice clasts were generated using μXCT with a ZEISS Xradia Versa 410 at the Istituto Nazionale di Geofisica e Vulcanologia-Osservatorio Vesuviano (Italy). A single ash particle within the 0/-0.5 φ (1-1.4 mm) grain size range was randomly selected from each of the bottom (KF176-C), bottom half (KF176-F), middle (KF176-I), and top (KF176-O), horizons of the type section. Additionally, a tubular pumice particle (Marti et al., 1999) was selected from the top half horizon (KF176-L) for textural comparison (**Fig. 3**).

The particles were cleaned using an ultrasonic bath before being scanned with μXCT. The field of view was configured to capture nearly the entire volume of each clast, and the working distance was adjusted to maximise resolution. Additionally, a 10x magnification lens was positioned before the detector to optically enhance the resolution, resulting in a final pixel size of 2 μm/px (8 μm^3/voxel). A total of 4001 bidimensional X-ray absorption projections were collected during a 360° rotation of the sample at 80 kV and 7 W. For samples KF176-C, KF176-I, and KF176-O, an additional scan was performed at 150 kV and 10 W decreasing the working distance and using a 20x magnification lens—and consequently reducing the field of view—to obtain an improved resolution of 1.1 μm/px (~1.3 μm^3/voxel). When necessary, a low-energy (LE1) filter was used to minimise beam hardening. The scans were then reconstructed into tomographic volumes using the integrated XRM Reconstructor software.

Tomographic volumes were processed using Dragonfly software (Dragonfly 3D World, 2024). Initially, a U-Net2D super-resolution model (Ronneberger et al., 2015), based on deep-learning neural networks, was trained using correspondent high-resolution (1.1 μm/px) and low-resolution (2 μm/px) volumes and applied to all lower-resolution datasets (2 μm/px). This approach significantly improved these datasets which, due to their larger field of view, captured more extensive and representative volumes of the original particles while maintaining practical scanning times (Buono et al., 2023). The effectiveness of this approach was validated through visual inspection (**Fig. 3**).

Subsequently, glass, vesicles (voids), and phenocrysts were labelled using the U-Net2.5D segmentation model (**Fig. 3**; Ronneberger et al., 2015). For each dataset, the model was trained on at least five 2D areas that had been manually segmented assigning grey-scale values (proportional to phase X-ray absorption) to the corresponding phases. This approach, considering both grey-scale values and shape factors, significantly improves segmentation accuracy, particularly for thin glass walls. Model performance was evaluated by comparing the automated segmentation to manual segmentation in three validation areas per dataset, confirming its reliability. To account for open vesicularity, vesicles open to the clast exterior were virtually closed at their outlet using a maximum width of 70 μm as a threshold, which minimised artificial modifications of vesicle volumes.

Once glasses and vesicles were segmented, the distance-transformed watershed algorithm was applied to separate individual bubbles that had become connected during the final stages of bubble growth or due to the scanning resolution being insufficient to capture extremely thin glass walls (< 2 μm; **Fig. 3**). This procedure successfully identified most bubbles down to 2 μm (~2 px) in equivalent diameter. Labelled objects smaller than this threshold were excluded from the dataset, to prevent potential noise artefacts (Pappalardo et al., 2018; Liedl et al., 2019; Buono et al., 2020).

3.4. Conduit dynamic modelling

From the textural datasets, we retrieved several parameters that were used as inputs for models or as quantitative descriptors of conduit dynamics. Pumice vesicularity (ϕ) was defined as the percentage of volume occupied by vesicles relative to the total volume (i.e., voids + glass – phenocrysts), while vesicle connectivity as the percentage of a connected vesicle network (pre-watershed, see §3.3) relative to the total vesicle volume. Volumetric descriptors of the shape and size of each vesicle (post-watershed) were used to construct vesicle size distribution and vesicle population density trends that can be used to describe the nucleation process (Cashman and Mangan, 1994; Shea et al., 2010 and references therein). Vesicle number density (VND), a key parameter for estimating magma decompression rates from vesicle textures (e.g., Toramaru, 2006; Shea, 2017), was calculated by dividing the total number of vesicles (post-watershed) by the glass volume (Proussevitch et al., 2007). Decompression rates were computed using the model developed by Toramaru (2006) in its simplified version proposed by Shea (2017):

$$\frac{dP}{dt} = \left(\frac{N_V}{A \times 10^4}\right)^{\frac{2}{3}} \quad (1)$$

where N_V corresponds to VND (mm^{-3}) and A is a composition-dependent fitting constant (3±1.8 for phonolites and trachytes; Shea, 2017).

3.4.1. Supersaturation pressure

The supersaturation pressure of bubble nucleation (ΔP_{sat}), and the related nucleation pressure (P_n), were estimated for a given decompression rate by integrating nucleation rates for progressive decompression steps (t_i in Eq. (3) in Mourtada-Bonnefoi and Laporte, 2004) and iteratively recalculating the bubble number density (Eq. (4) in Mourtada-Bonnefoi and Laporte, 2004) until the latter overpassed the value of 1 mm^{-3} (Mourtada-Bonnefoi and Laporte, 2004; Shea, 2017). The nucleation rate of bubbles (J) at a given melt pressure (P_M) was calculated following the classical nucleation theory (Hirth et al., 1970; Shea, 2017):

$$J = \frac{2n_0^2 DV}{a_0} \cdot \sqrt{\frac{\sigma}{kT}} \cdot exp\left(-\frac{16\pi\sigma^3}{3kT(P_B - P_{SAT})^2}\theta\right) \quad (2)$$

where θ is a geometric factor equivalent to 1 or $0 < \theta < 1$ for homogeneous and heterogeneous nucleation respectively (Shea, 2017), and k is the Boltzmann constant (i.e., 1.38×10^{-23} $m^2 \cdot kg \cdot s^{-2} \cdot K^{-1}$). T (K) is the temperature of the melt at the reservoir conditions (1253 K; Cappelli et al., 2025*)*. The saturation pressure, P_{SAT} (Pa), was set to 92 MPa as determined using water saturation models (Cappelli et al., 2025), while P_B (Pa) is the internal pressure of an incipient bubble nucleus, iteratively calculated for each step of P_M (Shea, 2017; Buono et al., 2020). D ($m^2 \cdot s^{-1}$) is the diffusivity of the volatile phase in the melt, calculated for water in phonolitic and trachytic melts using the model of Fanara et al. (2013). The volume of volatile molecules V (m^{-3}) was calculated according to Eq. (5) in Shea (2017). The mean distance between volatile molecules in the melt, a_0 (m), was derived as $n_0^{-1/3}$, where n_0 ($mol \cdot m^{-3}$) represents the number density of volatile molecules. n_0 was determined using Eq. (6) in Shea (2017) with inputs derived from haüyne-hosted melt inclusion data (Cappelli et al., 2025) which provided initial dissolved water concentrations (i.e., 4.82 wt.% on average, converted to a single-oxygen mass fraction) and melt density (2250 kg·m^3 on average). Finally, σ (N·m^{-1}) corresponds to the surface tension that can be either calculated for homogeneous nucleation adopting the Eq. (13) from Shea (2017) or fixed at the average value of 0.025 N·m^{-1}, considering magnetite microlites as primary nucleation sites (Shea, 2017).

3.4.2. Volatile outgassing in a porous magma

Tortuosity measures the deviation of the flow path between two bubbles from a straight line along the flow direction. It is a critical parameter reflecting the roughness of a porous medium and is therefore directly related to its permeability. However, due to the highly intricate network of vesicles, it was computationally impractical to quantify tortuosity directly using Dragonfly's skeletonization on a volume sufficiently large to be representative of the datasets. As an alternative, we utilized the tortuosity factor (τ*), which quantifies the difference between diffusivity under laminar conditions (fully conductive) and the actual diffusivity through the porous medium (Epstein, 1989; Cooper et al., 2016). Tortuosity factor can be related to tortuosity through Archie's law (Eq. (4) in Degruyter et al., 2012). To calculate τ*, we used the MATLAB application *TauFactor*, which computes τ* along three mutually perpendicular directions on cuboid volumes (Cooper et al., 2016). These cuboids were extracted from labelled vesicle volumes (pre-watershed), selecting the largest possible cuboid for each dataset, always ensuring it was several orders of magnitude larger than the largest vesicle present in the dataset (Pappalardo et al., 2018).

Darcian permeability (m^2) across the above-mentioned cuboid volumes was calculated using the Kozeny-Carman relation (Rust and Cashman, 2004; Degruyter et al., 2012; Wei et al., 2018; Valdivia et al., 2022) along each of the three perpendicular directions:

$$k_D = \frac{\varphi^3}{cS^2\tau^2} \qquad (3)$$

where the square of tortuosity is calculated through Archie's law, φ is vesicularity, S (m^{-1}) is the surface area per unit volume of the vesicle network and c is the Kozeny constant for pores-controlled media (set to 8; Degruyter et al., 2012).

Key parameters describing the flow of volatiles through porous media (outgassing) and their coupling with magma ascent include the dimensionless Forchheimer (Fo) and Stokes (St) numbers (Rust and Cashman, 2004; Degruyter et al., 2012; Zhou et al., 2019; Valdivia et al., 2022 and references therein). The Forchheimer number is defined as the ratio between the inertial and viscous forces resisting the flow. Similar to Reynolds number, it characterises flow behaviour, with lower *Fo* values indicating laminar flow. It can be expressed as (Rust and Cashman, 2004; Degruyter et al., 2012 and references therein):

$$Fo = \frac{\rho_g v}{\mu_g} \cdot \frac{k_D}{k_I} \quad (4)$$

where ρ_g is the density of the volatile phase defined as $P_M/(RT)$ with R as the specific gas constant for water (461.4 J·kg^{-1}·K^{-1}; Degruyter et al., 2012) and P_M the pressure in the conduit at a given depth, iterated during decompression; μ_g is the viscosity of the volatile phase (15×10^{-5} Pa·s; Degruyter et al., 2012); v (m·s^{-1}) is the average magma ascent velocity, calculated as the ratio of the mean decompression rate to the magmastatic gradient in the conduit (approximated by the lithostatic gradient, 0.027 MPa·m^{-1}; Browne and Szramek, 2015); and k_I is the inertial permeability (Rust and Cashman, 2004; Zhou et al., 2019) derived from k_D using the relationship proposed by Gonnerman et al., (2017; Eq. (B1)).

The Stokes number is defined by the ratio of the response time of magma to the flow time of volatile phases (Degruyter et al., 2012) and at low values indicates strong coupling between volatiles and the ascending magma. *St* can be expressed as (Degruyter et al., 2012):

$$St = \frac{\frac{\rho_B k_D}{\mu_g}}{\frac{r}{v}} \quad (5)$$

where ρ_B (kg·m^{-3}) is the bulk density (melt + bubbles) and r is the radius of the conduit, set at an average value of 50 m (Fontijn et al., 2011).

4. Results

4.1. Vesicularity and vesicle metrics

Vesicularities determined from three-dimensional imaging are, on average, lower than values obtained using 2D analyses ($\bar{x}$ ~63% ±5% and 74% ±6% respectively) though, within each datasets (2D or 3D), no significant differences were detected across different stratigraphic horizons (**Table 1**). Despite this discrepancy between 2D and 3D datasets, the consistent values of vesicularity and VND in pumiceous ash (%RSD ~ 7%) observed from 2D imaging across a wide selection of clasts confirms that randomly selected single clasts were sufficiently representative for µXCT analysis. Connected vesicle networks consistently account for 99.9% of the total vesicularity.

Vesicularity estimated from 3D reconstructions is influenced by the selection of grey-scale threshold during segmentation; however, conservative manual segmentation demonstrates that this effect on total vesicularity is minimal (~5 vol%) and deep learning models effectively delineate vesicle contours, preserving even the thinnest vesicle walls detectable at the applied resolution. The method's reliability is further supported by the small differences (5-8%) between scans collected at 20x and 10x (improved with the super-resolution model) magnifications, confirming the robustness of the approach. The discrepancy between 2D and 3D analyses thus likely arises from the limitations of bidimensional sectioning and sample preparation (e.g., glass breakage), which struggles to accurately represent irregular vesicles, risking overestimation of vesicularity (Shea et al., 2010). Vesicularity of lapilli-sized clasts analysed with pycnometry methods ranges around 0.85 ±0.04 (**Supplementary Material**). This high degree of vesicularity may result from post-depositional bubble inflation, which is more likely in larger clasts due to prolonged cooling times (Thomas et al., 1994; Kaminski and Jaupart, 1997). This phenomenon is visually evident from the occurrence of millimetric to centimetric vesicles on clast surfaces, which can influence and potentially alter original vesicularity determinations (**Supplementary Material**).

VNDs derived from both 2D and 3D imaging datasets yield values on the order of (10^{14} m^{-3}), and are again consistent across different stratigraphic horizons. VND values from both datasets are reported in **Table 1**. In 3D reconstructed particles, vesicle volume distributions (VVDs) predominantly exhibit lognormal distributions, with unimodal modes—indicating the volumetrically most represented size—ranging from 28 (log(L) = - 1.55) to 57 (log(L) = -1.25) µm equivalent diameters (**Fig. 4; Table 2**). Vesicle size distributions (VSDs) exhibit curved trends with one or more break points and tend to level off at larger sizes (**Fig**. **5**). Such distributions are strongly influenced by the choice of bins, which, in this case, are linearly spaced and equivalent in number to the geometric binning used for VVDs (Shea et al., 2010). Artefact spikes or broken segments may appear as a result. However, VSD trends of the finest vesicles allow us to extrapolate angular coefficients and intercepts at L = 0 mm (**Fig. 5**; **Table 2**), which are useful for estimating vesicle growth at late nucleation and growth conditions (§5.2). Cumulative vesicle size distributions (CVSDs) follow exponential trends but exhibit slope breaks at the largest sizes (**Supplementary Material**). These may reflect difficulties in accurately representing the largest vesicles, potentially due to the effects of bubble coalescence (e.g., Blower et al., 2002; Pappalardo et al., 2018; Liedl et al., 2019). Size distribution descriptors derived from the stereological conversion of 2D textures are consistent with those obtained from 3D reconstructions (**Fig. 6; Supplementary Material**).

In 2D sections, vesicles are generally subrounded; however, larger vesicles tend to deform and flatten at contacts with neighbouring vesicles or adopt irregular polylobate shapes especially when coalesced (**Fig. 2**). The average vesicle sphericity of 3D datasets ranges between 0.64 and 0.74 with a narrow spread ($\pm 0.09 < 1\sigma < \pm 0.12$). Sphericity is also negatively correlated with vesicle size (equivalent sphere diameter), and larger vesicles tends to be more irregular (**Supplementary Material; Table 2**). While no significant differences are observed across the other horizons, the minimum sphericity value is observed in the tube pumice, where vesicles predominantly exhibit elongated shapes. The preferential orientation of vesicles is evident in pole figures representing the orientation density of the vesicle's major axis relative to three mutually perpendicular axes (**Supplementary Material**). Although most pronounced in tube pumice, other samples also show a mild preferential orientation.

4.2. dP/dt and ΔP_{sat}

Estimates of VND-based decompression rates (Shea, 2017) are consistent across stratigraphic horizons, ranging between 4.8 and 7 $MPa \cdot s^{-1}$ ($\pm 1\sigma$ 0.9 $MPa \cdot s^{-1}$). Only for the tube pumice we obtain a slightly lower value of 2.8 $MPa \cdot s^{-1}$ (**Table 3**). Such values are also within the same order of magnitude—though slightly lower—of estimates provided by stereologically converted 2D VND, which have an average of 7.5 ±1.5 $MPa \cdot s^{-1}$. Decompression rates obtained using the embayment speedometer were evaluated across a range of initial exsolved water contents and final quenching pressures, according to the minimum least error (Georgeais et al., 2021). The resulting rates are of the same order of magnitude as those derived from vesicle texture analyses ($\overline{x}$ =4.7 ±2.7 $MPs \cdot s^{-1}$; **Table 3; Fig. 7**). An initial exsolved water content of ~3.6 wt.% consistently provided the best fits, with final quenching pressures ranging around 17 MPa (**Supplementary Table 1**).

The minimum ΔP_{sat} required for homogeneous bubble nucleation, determined for the range of decompression rates, was consistently ~52 MPa. Given an initial saturation pressure at conduit base of 92 MPa, this corresponds to a nucleation pressure of ~40 MPa (**Table 3**). Considering a broader reservoir pressure range—from the higher (107 MPa) to the lower (77 MPa) estimate first standard deviations—the resulting nucleation pressures span from 52 to 27 MPa, while the supersaturation pressure closely floats around 50 MPa. In contrast, assuming a heterogeneous nucleation regime, a significantly lower ΔP_{sat} of ~16 MPa (P_n~76 MPa) was obtained due to reduced surface tension. Considering the lack of microlites or nanolites, and the low abundance of phenocrysts, hereafter saturation pressures estimated through homogeneous nucleation were considered more plausible than heterogeneous ones (§5.2) and used for calculations.

4.3. Volatile outgassing

The tortuosity factor for "standard" clasts ranges from 1.70 to 3.78 and is consistent for the three directions investigated ($\pm 1\sigma = 0.12$ to 0.72). In contrast, the tube pumice exhibits much greater heterogeneity, with a relative standard deviation of 50% between the directions orthogonal to the major elongation of vesicles and the one parallel to it. A similar observation comes from Darcian permeability of clasts, which overall ranges from 1.27×10^{-13} and 1.27×10^{-12} m^2, and between 1.18×10^{-14} and 7.48×10^{-13} m^2 for the tube pumice, showing a relative standard deviation of 125% (**Table 3**).

Stokes and Forchheimer numbers are calculated using the average of Darcian permeability across each direction, except for the tube pumice where the maximum value was used to account for its anisotropy. For the other samples, Stokes numbers range from 5.08×10^{-5} and 6.85×10^{-4} (**Table 3**), indicating significant gas-melt coupling (**Fig. 8**; Rust and Cashman, 2004; Degruyter et al., 2012). Forchheimer number calculations were iterated between the estimated nucleation pressure (40 MPa) and a minimum quenching pressure of 17 MPa, and consistently exceeded a value of 10^3, suggesting a predominantly turbulent and hindered flow of volatiles through magma vesicularity (Degruyter et al. 2012).

5. Discussion

Upon ascent, magma undergoes rapid decompression, leading to volatile saturation and potentially, crystallisation. Bubble nucleation will occur only after reaching a critical level of volatile supersaturation, which depends on factors such as magma properties and volatile diffusivity in the melt and can be favoured by the availability of nucleation sites like microscopic or nanoscopic crystals (Shea, 2017; Cáceres et al., 2022). Alternatively, if significant crystallisation occurs at the reservoir level, incipient degassing may initiate magma ascent at greater depths due to second boiling (Edmonds and Woods, 2018). Following nucleation, bubbles grow, vesiculating and accelerating the melt-gas-crystalline mixture.

Depending on the interplay between parameters such as melt viscosity and ascent rate, bubbles may either rise faster than the melt (open-system degassing) or remain coupled with it (closed-system degassing). Closed-system degassing results in the formation of an expanded foam (e.g., Sparks, 1978; Proussevitch et al., 1993). As the foam grows, bubbles come into contact, and their connecting walls may collapse, leading to coalescence into larger bubbles and potentially to the formation of a connected network (Rust and Cashman, 2011; Degruyter et al., 2012; Burgisser et al., 2017). If the network achieves sufficient permeability, open-system degassing may occur, otherwise, particularly at high ascent velocities, outgassing is hindered. As the system continues to ascend, magma eventually fragments into discrete particles, or pyroclasts, which are violently ejected from the volcanic vent. Hereafter we explore the processes contributing to the explosivity of the Rungwe Pumice (RP) eruption, from bubble nucleation to magma fragmentation.

5.1. Sustained activity during the RP eruption

Plinian-style eruptions are characterised by the violent ejection of pyroclastic materials and could last for hours or even days, maintaining a steady mass discharge rate (MDR; Cioni et al., 2015 and references therein). Change in MDR during a prolonged eruption may occur due to factors such as reservoir replenishment, conduit widening, or variations in volatile concentrations (e.g., Carey and Sigurdsson, 1989). MDR fluctuations can be identified at the outcrop scale—where they may manifest as grading in fallout deposits or the onset of pyroclastic fountaining, which generates pyroclastic density currents—but are also preserved in textures of pumiceous products.

The pyroclastic fall deposit of the RP eruption is reversely graded at the base, suggesting an initial intensification of eruptive explosivity (Fontijn et al., 2011). Above that, the deposit is massive up to the top and lacks evidence of widespread PDCs descending the volcano's flanks. This suggests sustained eruptive activity throughout the event (Fontijn et al., 2011), despite we cannot exclude that not preserved or documented small PDCs interested the volcano summit (within a travel distance of 1-2 km; Fontijn et al., 2011). To evaluate whether these stable eruption conditions are also reflected in unaltered ascent rates and dynamics of bubble nucleation and growth, we analysed eruptive products collected from different horizons of the deposit, spanning its vertical extent.

Overall, VND, vesicularity, inferred magma decompression rate and outgassing parameters (**Table 3**) do not significantly vary between different horizons of the deposit (**Fig 9**). Peak MDRs for each horizon were estimated based on decompression rates using Eq. (16) of Shea (2017) and a constant conduit radius of 50 m (Fontijn et al., 2011). MDRs appear consistent across different horizons (**Table 3**) and averagely higher than the previously estimated range

(2.8-4.8×10^8 kg·s^{-1}) based on the eruptive column height inferred from tephra fallout dispersal patterns (Fontijn et al., 2011). Sample KF176I (middle horizon) exhibits the highest VND, with a larger proportion of smaller vesicle sizes than other samples (**Fig. 5**), and yields the highest explosivity score, calculated as the average of min-max normalised values of interdependent parameters indicative of explosivity (i.e., decompression rate and Darcian permeability; **Fig. 9**). However, values of main eruptive parameters remain within the same order of magnitude and maintain an average z-score within 1σ (**Fig. 9**). This slight deviation could therefore either attributed to an eruptive peak of relatively faster ascent rate, or to natural variability in the magmatic foam. However, these observations suggest that bubble evolution processes and fragmentation mechanisms were largely unaltered throughout the RP eruption.

The 3D textures of vesicles in tube pumice show slightly lower VND—however still within the same order of magnitude—and surface area per unit volume, resulting in an estimated decompression rate approximately half that of the “standard” ash samples. The tube pumice sample also displays the strongest iso-orientation of vesicles (**Fig. 10**; **Supplementary Material**), which are predominantly larger in size, along with the highest variability in permeability and outgassing efficiency across the three investigated directions (**Table 3**). These characteristics are associated with high shear conditions occurring along the conduit walls, where friction with the bedrock is maximal and promotes elongated bubble channels, particularly at high ascent rates (Marti et al., 1999; Mastin, 2005). However, these frictional forces also act to slow the ascent, generating a radial gradient in ascent velocity, explaining the lower estimated decompression rate (Gonnermann and Manga, 2003). As tube pumices are found throughout all horizons (on average 5 ±2% of components; Fontijn et al., 2011; Cappelli et al., 2025), they are interpreted as a product of localised enhanced shear stresses rather than evidence of changing ascent conditions.

5.2. Bubble nucleation and growth dynamics

Ascent velocity of magma in the conduit is a pivotal factor influencing many parameters, from bubble nucleation to outgassing efficiency (e.g., Gonnermann and Manga, 2007; Cassidy et al., 2018 and references therein). Decompression rates derived from VND-based model (5.9 ±0.9 MPa·s^{-1}) align with values reported previously for violent explosive Plinian-style eruptions of similar composition (**Fig. 7**; e.g., Shea, 2017; Cassidy et al., 2018 and references therein). These rates likely correspond to peak values (Shea, 2017), as magma accelerates drastically until fragmentation and quenching occur. These estimated rates are on average slightly higher than those inferred from embayment speedometry (4.7 ±2.7 $MPa \cdot s^{-1}$), which instead record an average decompression rate across the whole conduit (Hosseini et al., 2023). VND values used—which are on the order of 10^{14} m^{-3}—are consistent with values previously obtained for products of Plinian-style explosive eruptions (e.g., Humphreys et al., 2008; Rust and Cashman, 2011; Shea, 2017; Buono et al., 2020 and references therein). However, we acknowledge that the automated watershed algorithm may underestimate VND due to its inability to fully reconnect bubble walls lost during coalescence. Nevertheless, hypothetically doubling the number of bubbles would not change the order of magnitude of VND or decompression rates. Thus, this methodological underestimation of VND likely has minimal impact on decompression rate estimates, especially considering consistency with 2D datasets. Assuming a constant magmastatic gradient equivalent to the average lithostatic gradient (0.027 $MPa \cdot m^{-1}$), we estimate an average ascent velocity of 218 $m \cdot s^{-1}$. Such rapid ascent may counteract the diffusivity-dependent bubble nucleation and growth processes and consequently the degassing-induced microlite crystallisation.

The absence of microlites and the small amount of phenocrysts (≤ 0.03 vol.%) suggest that the bubble nucleation process predominantly occurred homogenously. Nanolites of iron-titanium oxides, undetectable at the µXCT resolution used, could potentially serve as sites for bubble nucleation (Shea, 2017; Cáceres et al., 2022). However, no such features were observed even at the highest magnification during SEM imaging (0.04 µm/pixel). Moreover, the characteristic Raman spectral peak at ~690 cm^{-1} associated with iron-bearing nanolites (Di Genova et al., 2017) was not detected in any of the embayments, including at their most external mouths. This suggests it is unlikely that nanolites would be widely present in the RP glass, and supports the hypothesis that nucleation initiated homogeneously and relatively late in the conduit, under conditions of high supersaturation pressure and at shallow depths.

We estimated a homogeneous supersaturation pressure for bubble nucleation of approximately 52 MPa, based on an initial reservoir pressure of 92 MPa, which corresponds to a nucleation pressure of 40 MPa. This significantly limits the time available for nucleation and growth. Decompression experiments demonstrated that a supersaturation pressure of ~50 MPa is sufficient to trigger homogeneous nucleation in evolved alkaline melts, as opposed to much higher ΔP_{sat} required in rhyolitic subalkaline or calcalkaline melts (100-180 MPa; Shea, 2017; Buono et al., 2020). In alkaline melts, the bubble number density peak (i.e., VND final order of magnitude) is almost reached within the first nucleation event at $\Delta P_{sat} \leq$ 50MPa (Mourtada-Bonnefoi and Laporte, 2004; Buono et al., 2020). Further decompression may increase the

VND by 1-2 orders of magnitude through multiple or continuous nucleation events (Mourtada-Bonnefoi and Laporte, 2004; Gonnermann and Manga, 2007; Buono et al., 2020), which coupled with bubble growth, eventually culminates in bubble coalescence and fragmentation.

The available time for bubble growth is therefore constrained between the nucleation depth (~1.9 km equivalent to a magmastatic pressure of 40 MPa) and the fragmentation level. Water concentrations measured at the embayment mouths should theoretically reflect the final water saturation in the melt before quenching, therefore being indicative of the fragmentation depth. However, water exsolution into bubbles depends on diffusivity and can be delayed if the ascent rate is particularly rapid. Additionally, surface imperfections at rims of polished glass embayments restricted Raman measurements to a few micrometres inside them, leading us to interpret saturation pressures from these measurements (29 ±7 MPa on average; **Supplementary Material**) as indicative of a minimum fragmentation depth. An alternative estimate comes from interpolating the best-fitting decompression path modelled to zero distance using EMBER. This approach yields an average final quenching pressure of ~17 MPa, indicating limited bubble growth time as nucleation began near 40 MPa.

VSDs and VVDs indicate continuous nucleation and growth under disequilibrium degassing conditions (Cashman and Mangan, 1994; Klug and Cashman, 1994; Blower et al., 2001, 2002; Shea et al., 2010), with minor bubble coalescence effects that flatten the VSD curves in the larger size regions, particularly evident in bottom half horizon (**Fig. 5**). The small equivalent diameter of the modes indicates a fine vesicularity (**Table 2**), confirming the limited time available for bubble growth. Using the time for bubble nucleation and growth (t), calculated assuming a constant ascent rate between 40 and 17 MPa, an average growth rate (G) of 1.76 $\times 10^{-3}$ mm·s^{-1} was estimated via the relation $a = -1/Gt$, where a is the angular coefficient of higher VSD trends (**Fig. 5**; Cashman and Mangan, 1994; Klug and Cashman, 1994; Klug et al., 2002). Peaks in bubble growth rates have been modelled at up to 0.1 mm·s^{-1} for rhyolitic melts (Proussevitch and Sahagian, 1998). In contrast, the lower growth rates observed in the RP suggest that bubble nucleation dominated over bubble growth even during the last stages of ascent. The exponential form of CVSDs further supports continuous bubble nucleation during ascent, driven by decompression-induced disequilibrium (Blower et al., 2001, 2002). However, as these CVSDs are not able to develop a full power-law trend, it implies a limited number of nucleation events (< 5; Blower et al., 2001), likely due to insufficient time or volatile supersaturation for formation of new bubbles to fill void spaces within growing ones in the final ascent stages. This suggests that VND was rapidly established mainly during early nucleation events of bubbles, which had limited time to grow. As bubbles came into contact with each other, they began to coalesce resulting in a poorly organised packing of approximately equally sized bubbles (Blower et al., 2001). This ultimately produced a relatively low-vesicularity bubble suspension, falling below the critical 0.75 vesicularity threshold typical of pumice lapilli produced during Plinian eruptions (Proussevitch et al., 1993; Cashman and Mangan, 1994).

The VSDs of de-coalesced datasets represent bubble conditions before the final stages of coalescence (Klug and Cashman, 1994). These suggest that during the early stages of bubble formation, coalescence played a minor role. However, as bubbles grew, they eventually interconnected into a complex vesicle network. Despite this, the limited time available hindered the development of sufficient permeability, preventing efficient outgassing (**Fig. 8**). Permeability pathways are not even developed at the conduit walls, where bubble stretching—maximised by shear—potentially favours gas escape through the channelling of iso-oriented bubbles. Tube pumice outgassing parameters (§3.4.2.) estimated along the primary elongation axis are comparable to those of "standard" foamed pumice. As a result, closed-system degassing persisted, maintaining coupled magma-gas ascent that intensified the internal pressure buildup, directly contributing to the violent fragmentation observed during the RP eruption. The combination of rapid nucleation, limited time for growth, and restricted permeability created a system primed for explosive fragmentation.

5.3. Fragmentation criterion

We exclude the influence of external factors such as the input of external water or sudden decompression due to edifice collapse in promoting fragmentation and eruption explosivity, as no evidence for these processes exists in the RP tephrostratigraphic record (Fontijn et al., 2011, 2013; this study). For viscous magmas unaffected by external gases or liquid water inputs, several fragmentation criteria have been proposed to produce explosive eruptions. However, fragmentation of peralkaline magmas is complex to evaluate with conventional criteria (e.g., Shea et al., 2017) and has been associated with a combination of localised strain, bubble overpressure, and a critical bubble volume fraction (e.g., Polacci et al., 2004; Hughes et al., 2017; Pappalardo et al., 2018; Stabile et al., 2021). To explore the conditions that led to explosivity during the RP eruption, we discuss four key fragmentation criteria: i) the bubble's critical volume fraction criterion (Sparks, 1978); ii) the strain-rate criterion (Dingwell and Webb, 1989; Dingwell, 1996; Papale, 1999); iii) the conduit-walls shear zone criterion

(Gonnermann and Manga, 2003); and iv) the bubble overpressure criterion (Zhang, 1999; Spieler et al., 2004; Mueller et al., 2008).

The bubble's critical volume fraction criterion foresees that a magmatic foam reaches instability once the gas phase occupies a critical volume fraction of ≥ 0.75 (Sparks, 1978; Gonnermann, 2015; Pappalardo et al., 2018). At this threshold, bubble walls stretch and thin to the point of rupture, leading to foam collapse that initiates at the surface through bubble bursting and then generates a downward propagating fragmentation level. Within the foam, bubbles achieve a high degree of interconnectivity. If outgassing is inefficient and slower than the magmatic ascent rate, this porosity threshold can be reached given sufficient time for bubble expansion (Sparks, 1978; Gonnermann, 2015). For the RP eruption, measurements indicate low Stokes and high Forchheimer numbers, suggesting coupled magma-gas ascent and a turbulent gas flow in magma vesicularity (Degruyter et al., 2012). These conditions, combined with high ascent rates and the magma's low permeability (even in flow-aligned tube pumices), imply inhibited outgassing during ascent (e.g., Degruyter et al., 2012; Valdivia et al., 2022; Bamber et al., 2024). However, none of the analysed pumice clasts reached the critical vesicularity threshold of 0.75 (**Table 1**). This makes the critical volume fraction criterion ineffective in this case, likely due to the limited time available for bubble expansion.

The strain rate criterion is based on the effects of prolonged and rapid elongational strain, induced by magma acceleration during ascent, on the structural response of magma (Dingwell and Webb, 1989; Dingwell, 1996; Papale, 1999). In this context, fragmentation is associated with crossing the glass transition threshold which occurs when the strain rate exceeds the structural relaxation time of the magma (Dingwell and Webb, 1989; Dingwell, 1996; Papale, 1999; Gonnermann, 2015). This transition marks a shift from viscous to elastic behaviour, eventually leading to brittle failure (Gonnermann, 2015). Fragmentation can result from either a drop in temperature below the glass transition temperature or from a sudden increase in the deformation rate (Dingwell and Webb, 1989). The strain rate criterion can be described through the Maxwell relation, where the critical strain rate (γ_{crit}) is related to the reciprocal of the relaxation time (τ) by the constant k =0.01 (Papale, 1999):

$$\gamma_{crit} = k\frac{1}{\tau} \tag{6}$$

During ascent, the elongational strain rate depends on magma acceleration and is described as dv_z/dz, or rather the dependency of magma ascent rate (v) with depth (z), where z = 0 m at the base of the conduit and increases upward. The structural relaxation time is linked to magma viscosity (μ) through the elastic modulus G = 10 GPa (Gonnermann and Manga, 2003), therefore the fragmentation criterion can be written as (Papale, 1999):

$$\frac{dv_z}{dz} > k\frac{G}{\mu} \tag{7}$$

For the RP, assuming a linear acceleration of magma from z = 0 m (P ~92 MPa) with an initial velocity v_0 = 0 m·s^{-1} to peak ascent rate of 218 m·s^{-1} (based on pumice textures recording the maximum ascent rate at fragmentation) at z = 2777 m (P ~17 MPa), we can estimate an average strain rate of 0.08 s^{-1}. Considering the relaxed viscosity (10^2-10^3 Pa·s), calculated for the RP compositions using the model of Giordano et al., (2008), at initial water concentrations (i.e., 4.82 wt.%) and temperatures (i.e., 925-975 °C), the criterion cannot be satisfied (**Fig. 11a-b**).

Upon ascent, magma rheology drastically changes due to processes such as water exsolution and bubble expansion cooling (Mastin and Ghiorso, 2001; Gonnermann and Manga, 2007), leading to an overall increase in magma viscosity by 2-3 orders of magnitude. Different processes significantly influence magma temperature (Mastin and Ghiorso, 2001; Gonnermann and Manga, 2007 and references therein): while friction at the conduit walls may heat the system, cooling effects like melt and gas expansion, as well as gas exsolution, dominate, especially in fast ascending magmas with large conduit radius. The system therefore can be subjected to an overall cooling trend, with gas temperature decreasing by up to 500 °C over a 50 MPa decompression (Mastin and Ghiorso, 2001). A simplified temperature balance can be derived by considering a single-phase, perfect gas system, where only the gas expansion effect is accounted for, as outlined in Eq. (21) of Mastin and Ghiorso (2001). This simplification excludes the contributions from melt expansion and gas exsolution, which together account for only 10–15% of the total cooling. Although decompression-induced microlite crystallisation could theoretically generate a heating effect counteracting gas exsolution undercooling (Mastin and Ghiorso, 2001; Blundy et al., 2006), syn-eruptive microlite crystallisation in RP magmas was extremely limited, preventing any significant crystallisation-related heating. using this approach, we estimated a minimum temperature drop up to ~200 °C for magma ascending from pressures of 40 MPa to 17 MPa.

We therefore tested the strain rate criterion for a temperature drop down to 725 °C and a gradient of water content spanning the concentrations recorded in melt embayments. Additionally, we also evaluated the water concentration potentially reached by the melt at the inferred quenching pressure of 17 MPa (i.e., ~1.05 wt.%), estimated by Di Matteo et al. (2004) solubility model. Even under the most extreme conditions, lowest water content and highest degree of cooling, the criterion remains unsatisfied (**Fig. 11a-b**). This may indicate that the magma viscosity of these compositions is generally too low to induce strain rate-dependent fragmentation caused solely by ascent-induced elongation.

We acknowledge that the assumption of linear acceleration is problematic, as conduit flow dynamic models suggest that ascent rates increase dramatically at shallow depths (Papale, 1999; Gonnermann and Manga, 2003, 2007; Campagnola et al., 2016; La Spina et al., 2021) when buoyancy forces of the foam are maximal, producing much higher localised strain rates. However, to satisfy the criterion at 725 °C and at fully degassed conditions (i.e., minimum water content at quenching), a minimum strain rate of 3.90 s^{-1} would be required. This corresponds to a significant acceleration occurring only within the last ~55 m below the fragmentation surface, which appears unrealistic.

The conduit wall shear zone criterion governs fragmentation at the melt-bedrock interface due to frictional forces created by the viscous flow of magma (Gonnermann and Manga, 2003). Shear-induced fragmentation occurs locally at the conduit walls when stress concentrates for an extended period, inducing a non-Newtonian response in the liquid and leading to the breakup of molecular bonds in a shear-thinning process (Dingwell, 1996; Gonnermann and Manga, 2003; Gonnermann, 2015). However, this localized process does not always generate explosive eruptions. In some cases, it can increase permeability and facilitate outgassing through melt and bedrock fractures, which may promote effusive rather than explosive behaviour (Gonnermann and Manga, 2003).

Like the strain-rate criterion, the shear zone criterion is dependent on melt viscosity at zero frequency and shear-strain rate, which is linked to conduit geometry, as postulated by Gonnermann and Manga (2003):

$$\frac{Q}{\pi R^3} \approx CG\mu_{crit}^{-0.9} \tag{8}$$

where Q is the volumetric flow rate ($m^3 \cdot s^{-1}$) through a cylindrical conduit of radius R (m), C is a fitting parameter equal to 0.01 $(Pa \cdot s)^{-0.1}$, and G = 10 GPa is the elastic modulus at infinite frequency. The fragmentation criterion is satisfied when melt viscosity exceeds the critical viscosity (μ_{crit}).

For the RP eruption, Q is obtained by dividing the MDR by the bulk density (melt+bubbles) of the magma. The bulk density is derived from the melt density (e.g., 2250 kg·m^{-3}; Cappelli et al., 2025) multiplied by the average vesicularity of ash (0.63). The conduit radius was ranged between 50 and 60 m (Fontijn et al., 2011) to evaluate its effect on μ_{crit} (the lowest value correspondent to R= 50 m is shown in **Fig. 11c**). The resulting critical viscosity is extremely high (~10^8 Pa·s) and cannot be exceeded even for minimum water contents and a temperature drop to 725 °C (**Fig. 11c**). Furthermore, fragmentation at conduit walls could have been mitigated by the cogenetic effect of viscous dissipation heating (Mastin, 2005) or by the lubricating action of compressible fusiform bubbles—as indicated by the presence of tube pumices in the deposit—which dissipated shear stress. Additionally, no evidence of shear-produced banded obsidians, indicative of prolonged cycles of fragmentation, deformation, and reannealing, (Gonnermann and Manga, 2003), was found in the deposit. While we cannot exclude that such a process occurred locally at conduit margins, it was most likely ineffective in triggering the fragmentation of the entire system.

The bubble overpressure criterion predicts magma fragmentation when the gas pressure inside bubbles exceeds the tensile strength of the magma, causing bubble-wall failure (Zhang, 1999; Gonnermann and Manga, 2003; Spieler et al., 2004; Mueller et al., 2008). During magma ascent, bubbles expand due to volatile diffusion and decompression. However, if this expansion is hindered or retarded by factors such as viscous resistance, surface tension, or volumetric constraints, bubbles can develop internal overpressure in disequilibrium with the melt pressure (Zhang, 1999). In viscous magmas, bubbles rise at the same rate as the surrounding melt, limiting the overpressure dissipation through outgassing. This buildup of overpressure can lead to an energetic release once it surpasses a critical instability threshold, triggering fragmentation and propagating a shock decompression wave downward through the conduit (Gonnermann, 2015). The growth of gas overpressure depends on the efficiency of outgassing, which is related to the permeability (k_D) and vesicularity (φ) of the magma. These parameters have been experimentally linked to the critical overpressure necessary for fragmentation by the relationship (Mueller et al., 2008):

$$\Delta P_{crit} = \frac{a\sqrt{k_D} + \sigma_m}{\varphi} \tag{9}$$

where a and σ_m are fitting parameters equivalent to 8.21 $\times 10^5$ MPa·m^{-1} and 1.54 MPa respectively.

To calculate the pre-fragmentation gas bubble overpressure for the RP eruption, we used a simplified Rayleigh-Plesset equation (Lensky et al., 2001; Gonnermann, 2015):

$$\Delta P = \frac{2\sigma}{r} + 4\mu \frac{G}{r} \quad (10)$$

which relates the bubble average radius r (m) to bubble growth rate G ($m \cdot s^{-1}$), where σ is the bubble surface tension, assumed to be ~0.1 $N \cdot m^{-1}$ (Gonnermann, 2015). We tested the criterion across a range of viscosities (μ), iteratively adjusting water concentration and temperature until the bubble overpressure exceeded the critical threshold of 3.54 ±0.21 MPa derived from Eq. (9). The criterion is satisfied for the minimum water concentrations recorded in the embayment glasses and for temperatures ≤ 725 °C, while for water contents at quenching pressure it results satisfied for temperatures of ~760 °C (**Fig. 11d**).

Bubble growth during magma ascent is controlled by diffusion-driven volatile exsolution and decompression-induced gas expansion. Water concentration gradients in embayments indicate that diffusion was not particularly effective in promoting exsolution. This is especially relevant considering that exsolution itself increases the viscosity of the melt around bubbles, thereby inhibiting further diffusion. As a result, gas expansion likely played a dominant role. However, we propose that growth was eventually limited, potentially restricting undercooling of the entire melt system. Instead, intense localised thermal gradients potentially formed at the bubble-melt interface inducing bubble wall rupture (Mastin and Ghiorso, 2001; Hughes et al., 2017), further supporting the bubble overpressure criterion.

In summary, we find that the bubble overpressure fragmentation criterion is satisfied, driven by drastic changes in melt viscosity induced by water exsolution and melt cooling. The conditions for RP explosivity are therefore linked to pre-eruptive water concentrations. Although these concentrations are lower than those observed in other phonolitic and trachytic systems (Carroll and Blank, 1997; Berndt et al., 2001; Romano et al., 2021), their combination with rapid ascent rates and initial overheating prevented microlite crystallisation and induced delayed bubble nucleation capable of forming an extremely energetic bubble suspension. We infer that the interplay between relatively shallow storage conditions and rapid ascent velocity was critical in governing magma behaviour. RP reservoir was likely destabilised by input of a volatile-rich magma from beneath (Fontijn et al., 2013; Cappelli et al., 2025). Such high ascent rates were possibly facilitated by the reservoir's relatively low density and viscosity, which allowed the rapid rise of hot, microlite-free, and pressurised magma. Shallow magmatic conditions are not unusual for phonolitic-trachytic reservoirs associated with explosive eruptions (e.g., Andújar et al., 2008; Scaillet et al., 2008). It has been documented how explosivity in such magmas is marked by the positive correlation of pressure and water concentration of reservoirs (Andújar and Scaillet, 2012), highlighting an interdependence between shallow conditions and low water content in driving explosive activity, even under undersaturated conditions (Andújar and Scaillet, 2012). The case for the RP eruption aligns with this trend while remaining unique in its specific conditions, offering a valuable comparison for other little-studied alkaline systems along the EAR that might share similar pre-eruptive shallow conditions.

6. Conclusions

In this study, we combined 2D and 3D textural methods with embayment water diffusivity-dependent speedometers to unravel the conduit processes driving the explosivity of the Rungwe Pumice eruption. We demonstrated how, during unrest, the rapid ascent of hot magma from shallow crustal levels inhibited microlite crystallisation. The absence of nucleation sites delayed bubble formation, leading to spontaneous nucleation at high supersaturation pressures. Energetic bubble nucleation outburst further accelerated magma ascent. However, bubble growth was constrained by the packing of bubbles into an intricate pore network and the limited time available before brittle fragmentation. This process led to bubble overpressure, which could not dissipate via outgassing through the vesicle network due to rapid ascent and insufficient time for the development of permeability pathways. Eventually, bubble overpressure overcame critical threshold when rheological changes induced by temperature drops and water exsolution—likely concentrated at bubble interconnections—allowed the brittle failure of the melt. Our model highlights the challenges in applying conventional fragmentation criteria to microlite-free and phenocryst-poor, relatively low-viscosity peralkaline magmas. In such systems, significant rheological alterations must be inferred to explain fragmentation. These findings suggest that further experimental work is essential to better characterise the fragmentation dynamics of these magmatic systems.

Acknowledgements

LC was founded by an F.R.S.-FNRS Aspirant grant. Samples were collected with support from Fonds Wetenschappelijk Onderzoek Aspirant Fellowship (2006-2010) awarded to KF; in this follow-up study, KF was supported by F.R.S.-FNRS MIS Grant F.451520F and PDR Grant

T.0121.24. µXCT analyses performed with funding from the European Union's Horizon Europe research and innovation program under grant agreement No 101131765 (EXCITE2) for Transnational Access conducted at Istituto Nazionale di Geofisica e Vulcanologia – Osservatorio Vesuviano (INGV-OV). The Raman equipment of KU Leuven was acquired via the medium-scale research infrastructure grant Raman-SIM2 (grant no I000718N).

Author contributions

This study was conceptualized by LC and KF. Data were collected by LC together with LP, GB, TDG, and VNS. Fieldwork was conducted by KF and facilitated by EM with contributions from SK, EA, and GGJE. LC handled data curation and drafted the manuscript. KF reviewed the first draft. All authors contributed to scientific discussion and manuscript revision.

References

Andújar, J., Costa, F., Martí, J., Wolff, J.A., Carroll, M.R., 2008. Experimental constraints on the pre-eruptive conditions of the phonolitic magma from the caldera-forming the Abrigo eruption, Tenerife (Canary Islands). Chem Geol 257, 173–191. https://doi.org/10.1016/j.chemgeo.2008.08.012

Andújar, J., Scaillet, B., 2012. Relationships between pre-eruptive conditions and eruptive styles of phonolite-trachyte magmas. Lithos 152, 122–131. https://doi.org/10.1016/j.lithos.2012.05.009

Arganda-Carreras, I., Kaynig, V., Rueden, C., Eliceiri, K.W., Schindelin, J., Cardona, A., Seung, H.S., 2017. Trainable Weka Segmentation: A machine learning tool for microscopy pixel classification. Bioinformatics 33, 2424–2426. https://doi.org/10.1093/bioinformatics/btx180

Bamber, E.C., La Spina, G., Arzilli, F., Polacci, M., Mancini, L., de' Michieli Vitturi, M., Andronico, D., Corsaro, R.A., Burton, M.R., 2024. Outgassing behaviour during highly explosive basaltic eruptions. Commun Earth Environ 5. https://doi.org/10.1038/s43247-023-01182-w

Berndt, J., Holtz, F., Koepke, J., 2001. Experimental constraints on storage conditions in the chemically zoned phonolitic magma chamber of the Laacher See volcano. Contributions to Mineralogy and Petrology 140, 469–486.

Blower, J.D., Keating, J.P., Mader, H.M., Phillips, J.C., 2002. The evolution of bubble size distributions in volcanic eruptions. Journal of Volcanology and Geothermal Research 120, 1–23.

Blower, J.D., Keating, J.P., Mader, H.M., Phillips, J.C., 2001. Inferring volcanic degassing processes from vesicle size distributions. Geophys Res Lett 28, 347–350. https://doi.org/10.1029/2000GL012188

Blundy, J., Cashman, K., Humphreys, M., 2006. Magma heating by decompression-driven crystallization beneath andesite volcanoes. Nature 443, 76–80. https://doi.org/10.1038/nature05100

Browne, B., Szramek, L., 2015. Rates of Magma Ascent and Storage, in: The Encyclopedia of Volcanoes. Elsevier, pp. 203–214. https://doi.org/10.1016/B978-0-12-385938-9.00009-2

Buono, G., Caliro, S., Macedonio, G., Allocca, V., Gamba, F., Pappalardo, L., 2023. Exploring microstructure and petrophysical properties of microporous volcanic rocks through 3D multiscale and super-resolution imaging. Sci Rep 13. https://doi.org/10.1038/s41598-023-33687-x

Buono, G., Fanara, S., Macedonio, G., Palladino, D.M., Petrosino, P., Sottili, G., Pappalardo, L., 2020. Dynamics of degassing in evolved alkaline magmas: Petrological, experimental and theoretical insights. Earth Sci Rev. https://doi.org/10.1016/j.earscirev.2020.103402

Burgisser, A., Chevalier, L., Gardner, J.E., Castro, J.M., 2017. The percolation threshold and permeability evolution of ascending magmas. Earth Planet Sci Lett 470, 37–47. https://doi.org/10.1016/j.epsl.2017.04.023

Cáceres, F., Scheu, B., Colombier, M., Hess, K.U., Feisel, Y., Ruthensteiner, B., Dingwell, D.B., 2022. The roles of microlites and phenocrysts during degassing of silicic magma. Earth Planet Sci Lett 577. https://doi.org/10.1016/j.epsl.2021.117264

Campagnola, S., Romano, C., Mastin, L.G., Vona, A., 2016. Confort 15 model of conduit dynamics: applications to Pantelleria Green Tuff and Etna 122 BC eruptions. Contributions to Mineralogy and Petrology 171. https://doi.org/10.1007/s00410-016-1265-5

Cappelli, L., Wallace, P.A., Ernst, G.G., Mbede, E., Kwelwa, S., Abdallah, E., Fontijn, K., 2025. Pre-eruptive reservoir conditions of the peralkaline Rungwe Pumice (Tanzania) Plinian eruption from haüyne-hosted melt inclusions. EarthArXiv [Preprint 8452]. 28-01-2025 [cited 28-01-2025]. https://doi.org/10.31223/X5513F

Carey, S., Sigurdsson, H., 1989. The intensity of plinian eruptions. Bull Volcanol 51, 28–40.

Carey, S., Sparks, R.S.J., 1986. Quantitative models of the fallout and dispersal of tephra from volcanic eruption columns. Bull Volcanol 48, 109–125. https://doi.org/10.1007/BF01046546

Carroll, M.R., Blank, J.G., 1997. The solubility of H_2O in phonolitic melts, American Mineralogist.

Cashman, K. V, Mangan, M.T., 1994. Chapter 11b. PHYSICAL ASPECTS OF MAGMATIC DEGASSING II. Constraints on vesiculation processes from textural studies of eruptive products, in: Carroll, M.R., Holloway, J.R. (Eds.), Volatiles in Magmas. De Gruyter, Berlin, Boston, pp. 447–478. https://doi.org/doi:10.1515/9781501509674-018

Cassidy, M., Manga, M., Cashman, K., Bachmann, O., 2018. Controls on explosive-effusive volcanic eruption styles. Nat Commun 9. https://doi.org/10.1038/s41467-018-05293-3

Cioni, R., 2000. Volatile content and degassing processes in the AD 79 magma chamber at Vesuvius (Italy). Contributions to Mineralogy and Petrology 140, 40–54. https://doi.org/10.1007/s004100000167

Cioni, R., Pistolesi, M., Rosi, M., 2015. Plinian and Subplinian Eruptions, in: The Encyclopedia of Volcanoes. Elsevier, pp. 519–535. https://doi.org/10.1016/b978-0-12-385938-9.00029-8

Cooper, S.J., Bertei, A., Shearing, P.R., Kilner, J.A., Brandon, N.P., 2016. TauFactor: An open-source application for calculating tortuosity factors from tomographic data. SoftwareX 5, 203–210. https://doi.org/10.1016/j.softx.2016.09.002

deGraffenried, R.L., Shea, T., 2021. Using Volatile Element Concentration Profiles in Crystal-Hosted Melt Embayments to Estimate Magma Decompression Rate: Assumptions and Inherited Errors. Geochemistry, Geophysics, Geosystems 22. https://doi.org/10.1029/2021GC009672

Degruyter, W., Bachmann, O., Burgisser, A., Manga, M., 2012. The effects of outgassing on the transition between effusive and explosive silicic eruptions. Earth Planet Sci Lett 349–350, 161–170. https://doi.org/10.1016/j.epsl.2012.06.056

Di Genova, D., Romano, C., Hess, K.U., Vona, A., Poe, B.T., Giordano, D., Dingwell, D.B., Behrens, H., 2013. The rheology of peralkaline rhyolites from Pantelleria Island. Journal of Volcanology and Geothermal Research 249, 201–216. https://doi.org/10.1016/j.jvolgeores.2012.10.017

Di Genova, D., Sicola, S., Romano, C., Vona, A., Fanara, S., Spina, L., 2017. Effect of iron and nanolites on Raman spectra of volcanic glasses: A reassessment of existing strategies to estimate the water content. Chem Geol 475, 76–86. https://doi.org/10.1016/j.chemgeo.2017.10.035

Di Matteo, V., Carroll, M.R., Behrens, H., Vetere, F., Brooker, R.A., 2004. Water solubility in trachytic melts. Chem Geol 213, 187–196. https://doi.org/10.1016/j.chemgeo.2004.08.042

Dingwell, D.B., 1996. Volcanic Dilemma: Flow or Blow? Science (1979) 273, 1054–1055.

Dingwell, D.B., Webb, S.L., 1989. Structural Relaxation in Silicate Melts and Non-Newtonian Melt Rheology in Geologic Processes. Phys Chem Miner 16, 508–516.

Dragonfly 3D World, 2024. for Windows; Comet Technologies Canada Inc., Montreal, Canada; software available at: https://www.theobjects.com/dragonfly.

Ebinger, C.J., Deino, A.L., Drake, E., Tesha, A.L., 1989. Chronology of volcanism and rift basin propagation: Rungwe Volcanic Province, East Africa. Journal of Geophysical Research 94, 15785–15803.

Ebinger, C.J., Deino, A.L., Tesha, A.L., Becker, T., Ring, U., 1993. Tectonic controls on rift basin morphology: evolution of the northern Malawi (Nyasa) Rift. J Geophys Res 98. https://doi.org/10.1029/93jb01392

Ebinger, C.J., Keir, D., Bastow, I.D., Whaler, K., Hammond, J.O.S., Ayele, A., Miller, M.S., Tiberi, C., Hautot, S., 2017. Crustal Structure of Active Deformation Zones in Africa: Implications for Global Crustal Processes. Tectonics. https://doi.org/10.1002/2017TC004526

Edmonds, M., Woods, A.W., 2018. Exsolved volatiles in magma reservoirs. Journal of Volcanology and Geothermal Research. https://doi.org/10.1016/j.jvolgeores.2018.10.018

Epstein, N., 1989. On tortuosity and tortuosity factor. Chemical EngineeringScience 44, 777–779.

Fanara, S., Behrens, H., Zhang, Y., 2013. Water diffusion in potassium-rich phonolitic and trachytic melts. Chem Geol 346, 149–161. https://doi.org/10.1016/j.chemgeo.2012.09.030

Fontijn, K., Delvaux, D., Ernst, G.G.J., Kervyn, M., Mbede, E., Jacobs, P., 2010a. Tectonic control over active volcanism at a range of scales: Case of the Rungwe Volcanic Province, SW Tanzania; and hazard implications. Journal of African Earth Sciences 58, 764–777. https://doi.org/10.1016/j.jafrearsci.2009.11.011

Fontijn, K., Elburg, M.A., Nikogosian, I.K., van Bergen, M.J., Ernst, G.G.J., 2013. Petrology and geochemistry of Late Holocene felsic magmas from Rungwe volcano (Tanzania), with implications for trachytic Rungwe Pumice eruption dynamics. Lithos 177, 34–53. https://doi.org/10.1016/j.lithos.2013.05.012

Fontijn, K., Ernst, G.G.J., Bonadonna, C., Elburg, M.A., Mbede, E., Jacobs, P., 2011. The ~4-ka Rungwe Pumice (South-Western Tanzania): A wind-still Plinian eruption. Bull Volcanol 73, 1353–1368. https://doi.org/10.1007/s00445-011-0486-8

Fontijn, K., Ernst, G.G.J., Elburg, M.A., Williamson, D., Abdallah, E., Kwelwa, S., Mbede, E., Jacobs, P., 2010b. Holocene explosive eruptions in the Rungwe Volcanic Province, Tanzania. Journal of Volcanology and Geothermal Research 196, 91–110. https://doi.org/10.1016/j.jvolgeores.2010.07.021

Fontijn, K., Williamson, D., Mbede, E., Ernst, G.G.J., 2012. The Rungwe Volcanic Province, Tanzania - A volcanological review. Journal of African Earth Sciences 63, 12–31. https://doi.org/10.1016/j.jafrearsci.2011.11.005

Garcin, Y., Williamson, D., Taieb, M., Vincens, A., Mathé, P.E., Majule, A., 2006. Centennial to millennial changes in maar-lake deposition during the last 45,000 years in tropical Southern Africa (Lake Masoko, Tanzania). Palaeogeogr Palaeoclimatol Palaeoecol 239, 334–354. https://doi.org/10.1016/j.palaeo.2006.02.002

Georgeais, G., Koga, K.T., Moussallam, Y., Rose-Koga, E.F., 2021. Magma Decompression Rate Calculations With EMBER: A User-Friendly Software to Model Diffusion of H2O, CO2, and S in Melt Embayments. Geochemistry, Geophysics, Geosystems 22. https://doi.org/10.1029/2020GC009542

Geshi, N., Yamasaki, T., Miyagi, I., Conway, C.E., 2021. Magma chamber decompression during explosive caldera-forming eruption of Aira caldera. Commun Earth Environ 2. https://doi.org/10.1038/s43247-021-00272-x

Ghiorso, M.S., Gualda, G.A.R., 2015. An H2O–CO2 mixed fluid saturation model compatible with rhyolite-MELTS. Contributions to Mineralogy and Petrology 169. https://doi.org/10.1007/s00410-015-1141-8

Giachetti, T., Burgisser, A., Arbaret, L., Druitt, T.H., Kelfoun, K., 2011. Quantitative textural analysis of Vulcanian pyroclasts (Montserrat) using multi-scale X-ray computed microtomography: Comparison with results from 2D image analysis. Bull Volcanol 73, 1295–1309. https://doi.org/10.1007/s00445-011-0472-1

Giordano, D., Dingwell, D.B., 2003. Viscosity of hydrous Etna basalt: Implications for Plinian-style basaltic eruptions. Bull Volcanol 65, 8–14. https://doi.org/10.1007/s00445-002-0233-2

Giordano, D., Russell, J.K., Dingwell, D.B., 2008. Viscosity of magmatic liquids: A model. Earth Planet Sci Lett 271, 123–134. https://doi.org/10.1016/j.epsl.2008.03.038

Gonnermann, H.M., 2015. Magma fragmentation. Annu Rev Earth Planet Sci 43, 431–458. https://doi.org/10.1146/annurev-earth-060614-105206

Gonnermann, H.M., Giachetti, T., Fliedner, C., Nguyen, C.T., Houghton, B.F., Crozier, J.A., Carey, R.J., 2017. Permeability During Magma Expansion and Compaction. J Geophys Res Solid Earth 122, 9825–9848. https://doi.org/10.1002/2017JB014783

Gonnermann, H.M., Manga, M., 2007. The fluid mechanics inside a volcano. Annu Rev Fluid Mech. https://doi.org/10.1146/annurev.fluid.39.050905.110207

Gonnermann, H.M., Manga, M., 2003. Explosive volcanism may not be an inevitable consequence of magma fragmentation. Nature 426, 432–435. https://doi.org/10.1038/nature02138

Gurioli, L., Andronico, D., Bachelery, P., Balcone-Boissard, H., Battaglia, J., Boudon, G., Burgisser, A., Burton, M.R., Cashman, K., Cichy, S., Cioni, R., Di Muro, A., Dominguez, L., D'Oriano, C., Druitt, T., Harris, A.J.L., Hort, M., Kelfoun, K., Komorowski, J.C., Kueppers, U., Le Pennec, J.L., Menand, T., Paris, R., Pioli, L., Pistolesi, M., Polacci, M., Pompilio, M., Ripepe, M., Roche, O., Rose-Koga, E., Rust, A., Schiavi, F., Scharff, L., Sulpizio, R., Taddeucci, J., Thordarson, T., 2015. MeMoVolc consensual document: a review of cross-disciplinary approaches to characterizing small explosive magmatic eruptions. Bull Volcanol 77. https://doi.org/10.1007/s00445-015-0935-x

Harkin, D.A., 1960. The Rungwe Volcanics at the Northern End of Lake Nyasa, 1st ed. Government Printer.

Hirth, J.P., Pound, G.M., St Pierre, G.R., 1970. Bubble Nucleation. Metallurgical Transactions I, 938–945.

Hosseini, B., Myers, M.L., Watkins, J.M., Harris, M.A., 2023. Are We Recording? Putting Embayment Speedometry to the Test Using High Pressure-Temperature Decompression Experiments. Geochemistry, Geophysics, Geosystems 24. https://doi.org/10.1029/2022gc010770

Houghton, B.F., Gonnermann, H.M., 2008. Basaltic explosive volcanism: Constraints from deposits and models. Chemie der Erde 68, 117–140. https://doi.org/10.1016/j.chemer.2008.04.002

Houghton, B.F., Wilson, C.J.N., Del Carlo, P., Coltelli, M., Sable, J.E., Carey, R., 2004. The influence of conduit processes on changes in style of basaltic Plinian eruptions: Tarawera 1886 and Etna 122 BC. Journal of Volcanology and Geothermal Research 137, 1–14. https://doi.org/10.1016/j.jvolgeores.2004.05.009

Hughes, E.C., Neave, D.A., Dobson, K.J., Withers, P.J., Edmonds, M., 2017. How to fragment peralkaline rhyolites: Observations on pumice using combined multi-scale 2D and 3D imaging. Journal of Volcanology and Geothermal Research 336, 179–191. https://doi.org/10.1016/j.jvolgeores.2017.02.020

Humphreys, M.C.S., Menand, T., Blundy, J.D., Klimm, K., 2008. Magma ascent rates in explosive eruptions: Constraints from H2O diffusion in melt inclusions. Earth Planet Sci Lett 270, 25–40. https://doi.org/10.1016/j.epsl.2008.02.041

Hutchison, W., Mather, T.A., Pyle, D.M., Boyce, A.J., Gleeson, M.L.M., Yirgu, G., Blundy, J.D., Ferguson, D.J., Vye-Brown, C., Millar, I.L., Sims, K.W.W., Finch, A.A., 2018. The evolution of magma during continental rifting: New constraints from the isotopic and trace element signatures of silicic magmas from Ethiopian volcanoes. Earth Planet Sci Lett 489, 203–218. https://doi.org/10.1016/j.epsl.2018.02.027

Iacovino, K., Matthews, S., Wieser, P.E., Moore, G.M., Bégué, F., 2021. VESIcal Part I: An Open-Source Thermodynamic Model Engine for Mixed Volatile (H2O-CO2) Solubility in Silicate Melts. Earth and Space Science 8. https://doi.org/10.1029/2020EA001584

Jochum, K.P., Stoll, B., Herwig, K., Willbold, M., Hofmiann, A.W., Amini, M., Aarburg, S., Abouchami, W., Hellebrand, E., Mocek, B., Raczek, I., Stracke, A., Alard, O., Bouman, C., Becker, S., Dücking, M., Brätz, H., Klemd, R., De Bruin, D., Canil, D., Cornell, D., De Hoog, C.J., Dalpé, C., Danyushevshy, L., Eisenhauer, A., Gao, Y., Snow, J.E., Groschopf, N., Günther, D., Latkoczy, C., Guillong, M., Hauri, E.H., Höfer, H.E., Lahaye, Y., Horz, K., Jacob, D.E., Kasemann, S.A., Kent, A.J.R., Ludwig, T., Zack, T., Mason, P.R.D., Meixner, A., Rosner, M., Misawa, K., Nash, B.P., Pfänder, J., Premo, W.R., Sun, W.D., Tiepolo, M., Vannucci, R., Vennemann, T., Wayne, D., Woodhead, J.D., 2006. MPI-DING reference glasses for in situ microanalysis: New reference values for element concentrations and isotope ratios. Geochemistry, Geophysics, Geosystems 7. https://doi.org/10.1029/2005GC001060

Kaminski, E., Jaupart, C., 1997. Expansion and quenching of vesicular magma fragments in Plinian eruptions. J Geophys Res Solid Earth 102, 12187–12203. https://doi.org/10.1029/97jb00622

Klug, C., Cashman, K., Bacon, C., 2002. Structure and physical characteristics of pumice from the climactic eruption of Mount Mazama (Crater Lake), Oregon. Bull Volcanol 64, 486–501. https://doi.org/10.1007/s00445-002-0230-5

Klug, C., Cashman, K. V., 1994. Vesiculation of May 18, 1980, Mount St. Helens magma. Geology 22, 468–472.

La Spina, G., Arzilli, F., Llewellin, E.W., Burton, M.R., Clarke, A.B., de' Michieli Vitturi, M., Polacci, M., Hartley, M.E., Di Genova, D., Mader, H.M., 2021. Explosivity of basaltic lava fountains is controlled by magma rheology, ascent rate and outgassing. Earth Planet Sci Lett 553. https://doi.org/10.1016/j.epsl.2020.116658

Legland, D., Arganda-Carreras, I., Andrey, P., 2016. MorphoLibJ: Integrated library and plugins for mathematical morphology with ImageJ. Bioinformatics 32, 3532–3534. https://doi.org/10.1093/bioinformatics/btw413

Lensky, N.G., Lyakhovsky, V., Navon, O., 2001. Radial variations of melt viscosity around growing bubbles and gas overpressure in vesiculating magmas. Earth Planet Sci Lett 186, 1–6.

Liedl, A., Buono, G., Lanzafame, G., Dabagov, S.B., Della Ventura, G., Hampai, D., Mancini, L., Marcelli, A., Pappalardo, L., 2019. A 3D imaging textural characterization of pyroclastic products from the 1538 AD Monte Nuovo eruption (Campi Flegrei, Italy). Lithos 340–341, 316–331. https://doi.org/10.1016/j.lithos.2019.05.010

Liu, Y., Anderson, A.T., Wilson, C.J.N., 2007. Melt pockets in phenocrysts and decompression rates of silicic magmas before fragmentation. J Geophys Res Solid Earth 112. https://doi.org/10.1029/2006JB004500

Macdonald, R., Scaillet, B., 2006. The central Kenya peralkaline province: Insights into the evolution of peralkaline salic magmas. Lithos 91, 59–73. https://doi.org/10.1016/j.lithos.2006.03.009

Marti, J., Soriano, C., Dingwell, D.B., 1999. Tube pumices as strain markers of the ductile-brittle transition in magma fragmentation. Nature 402, 650–653.

Mastin, L.G., 2005. The controlling effect of viscous dissipation on magma flow in silicic conduits. Journal of Volcanology and Geothermal Research 143, 17–28. https://doi.org/10.1016/j.jvolgeores.2004.09.008

Mastin, L.G., Ghiorso, M.S., 2001. Adiabatic temperature changes of magma-gas mixtures during ascent and eruption. Contributions to Mineralogy and Petrology 141, 307–321. https://doi.org/10.1007/s004100000210

Mourtada-Bonnefoi, C.C., Laporte, D., 2004. Kinetics of bubble nucleation in a rhyolitic melt: An experimental study of the effect of ascent rate. Earth Planet Sci Lett 218, 521–537. https://doi.org/10.1016/S0012-821X(03)00684-8

Mueller, S., Scheu, B., Spieler, O., Dingwell, D.B., 2008. Permeability control on magma fragmentation. Geology 36, 399–402. https://doi.org/10.1130/G24605A.1

Newhall, C.G., Self, S., 1982. The volcanic explosivity index (VEI): an estimate of the explosive magnitude for historical eruptions. J Geophys Res 87, 1231–1238.

Ni, H., Zhang, L., 2018. A general model of water diffusivity in calc-alkaline silicate melts and glasses. Chem Geol 478, 60–68. https://doi.org/10.1016/j.chemgeo.2017.10.010

Papale, P., 1999. Strain-induced magma fragmentation in explosive eruptions. Nature 397, 425–428.

Pappalardo, L., Buono, G., Fanara, S., Petrosino, P., 2018. Combining textural and geochemical investigations to explore the dynamics of magma ascent during Plinian eruptions: a Somma–Vesuvius volcano (Italy) case study. Contributions to Mineralogy and Petrology 173. https://doi.org/10.1007/s00410-018-1486-x

Pappalardo, L., Buono, G., Fanara, S., Yi, J., Shan, X., Guo, Z., Zhang, M., Ventura, G., 2023. The role of CO2 flushing in triggering the 'Millennium' eruption and recent unrests at Changbaishan volcano (China/North Korea). Int Geol Rev 65, 706–719. https://doi.org/10.1080/00206814.2022.2065544

Pappalardo, L., Mastrolorenzo, G., 2012. Rapid differentiation in a sill-like magma reservoir: A case study from the campi flegrei caldera. Sci Rep 2. https://doi.org/10.1038/srep00712

Polacci, M., Mancini, L., Baker, D.R., 2010. The contribution of synchrotron X-ray computed microtomography to understanding volcanic processes. J Synchrotron Radiat 17, 215–221. https://doi.org/10.1107/S0909049509048225

Polacci, M., Papale, P., Del Seppia, D., Giordano, D., Romano, C., 2004. Dynamics of magma ascent and fragmentation in trachytic versus rhyolitic eruptions. Journal of Volcanology and Geothermal Research 131, 93–108. https://doi.org/10.1016/S0377-0273(03)00319-6

Proussevitch, A.A., Sahagian, D.L., 1998. Dynamics and energetics of bubble growth in magmas: Analytical formulation and numerical modeling. J Geophys Res Solid Earth 103, 18223–18251. https://doi.org/10.1029/98jb00906

Proussevitch, A.A., Sahagian, D.L., Kutolin, V.A., 1993. Stability of foams in silicate melts, Journal of Volcanology and Geothermal Research.

Proussevitch, A.A., Sahagian, D.L., Tsentalovich, E.P., 2007. Statistical analysis of bubble and crystal size distributions: Formulations and procedures. Journal of Volcanology and Geothermal Research 164, 95–111. https://doi.org/10.1016/j.jvolgeores.2007.04.007

Romano, P., Di Carlo, I., Andújar, J., Rotolo, S.G., 2021. Water solubility in trachytic and pantelleritic melts: An experimental study. Comptes Rendus - Geoscience. https://doi.org/10.5802/CRGEOS.75

Ronneberger, O., Fischer, P., Brox, T., 2015. U-net: Convolutional networks for biomedical image segmentation, in: Lecture Notes in Computer Science (Including Subseries Lecture Notes in Artificial Intelligence and Lecture Notes in Bioinformatics). Springer Verlag, pp. 234–241. https://doi.org/10.1007/978-3-319-24574-4_28

Rust, A.C., Cashman, K. V., 2011. Permeability controls on expansion and size distributions of pyroclasts. J Geophys Res Solid Earth 116. https://doi.org/10.1029/2011JB008494

Rust, A.C., Cashman, K. V., 2004. Permeability of vesicular silicic magma: Inertial and hysteresis effects. Earth Planet Sci Lett 228, 93–107. https://doi.org/10.1016/j.epsl.2004.09.025

Saria, E., Calais, E., Stamps, D.S., Delvaux, D., Hartnady, C.J.H., 2014. Present-day kinematics of the East African Rift. J Geophys Res Solid Earth 119, 3584–3600. https://doi.org/10.1002/2013JB010901

Scaillet, B., Pichavant, M., Cioni, R., 2008. Upward migration of Vesuvius magma chamber over the past 20,000 years. Nature 455, 216–219. https://doi.org/10.1038/nature07232

Schindelin, J., Arganda-Carreras, I., Frise, E., Kaynig, V., Longair, M., Pietzsch, T., Preibisch, S., Rueden, C., Saalfeld, S., Schmid, B., Tinevez, J.-Y., White, D.J., Hartenstein, V., Eliceiri, K., Tomancak, P., Cardona, A., 2012. Fiji: an open-source platform for biological-image analysis. Nat Methods 9, 676–682. https://doi.org/10.1038/nmeth.2019

Schmidt, B.C., Blum-Oeste, N., Flagmeier, J., 2013. Water diffusion in phonolite melts. Geochim Cosmochim Acta 107, 220–230. https://doi.org/10.1016/j.gca.2012.12.044

Shea, T., 2017. Bubble nucleation in magmas: A dominantly heterogeneous process? Journal of Volcanology and Geothermal Research. https://doi.org/10.1016/j.jvolgeores.2017.06.025

Shea, T., Houghton, B.F., Gurioli, L., Cashman, K. V., Hammer, J.E., Hobden, B.J., 2010. Textural studies of vesicles in volcanic rocks: An integrated methodology. Journal of Volcanology and Geothermal Research 190, 271–289. https://doi.org/10.1016/j.jvolgeores.2009.12.003

Shea, T., Leonhardi, T., Giachetti, T., Lindoo, A., Larsen, J., Sinton, J., Parsons, E., 2017. Dynamics of an unusual cone-building trachyte eruption at Puʻu Waʻawaʻa, Hualālai volcano, Hawaiʻi. Bull Volcanol 79. https://doi.org/10.1007/s00445-017-1106-z

Sparks, R.S.J., 1978. The dynamics of bubble formation and growth in magmas: a review and analysis. Journal of Volcanology and Geothermal Research 3, 1–37.

Spieler, O., Kennedy, B., Kueppers, U., Dingwell, D.B., Scheu, B., Taddeucci, J., 2004. The fragmentation threshold of pyroclastic rocks. Earth Planet Sci Lett 226, 139–148. https://doi.org/10.1016/j.epsl.2004.07.016

Stabile, P., Arzilli, F., Carroll, M.R., 2021. Crystallization of peralkaline rhyolitic magmas: Pre- And syn-eruptive conditions of the Pantelleria system. Comptes Rendus - Geoscience. https://doi.org/10.5802/CRGEOS.72

Tadesse, A.Z., Fontijn, K., Wallace, P.A., Gurioli, L., Laha, P., Terryn, H., Ayalew, D., 2024. Eruption style and dynamics of the ~ 87 ka Baricha peralkaline rhyolite eruption in Ethiopia. Bull Volcanol 86. https://doi.org/10.1007/s00445-024-01787-9

Thomas, N., Jaupart, C., Vergniolle, S., 1994. On the vesicularity of pumice. J Geophys Res 99. https://doi.org/10.1029/94jb00650

Toramaru, A., 2006. BND (bubble number density) decompression rate meter for explosive volcanic eruptions. Journal of Volcanology and Geothermal Research 154, 303–316. https://doi.org/10.1016/j.jvolgeores.2006.03.027

Valdivia, P., Marshall, A.A., Brand, B.D., Manga, M., Huber, C., 2022. Mafic explosive volcanism at Llaima Volcano: 3D x-ray microtomography reconstruction of pyroclasts to constrain shallow conduit processes. Bull Volcanol 84. https://doi.org/10.1007/s00445-021-01514-8

Van Gerve, T.D., Namur, O., 2023. SilicH2O: a graphical user interface for processing silicate glass Raman spectra and quantifying H2O. Volcanica 6, 405–413. https://doi.org/10.30909/vol.06.02.405413

Wallace, P.A., Otieno, V., Godec, P., Njoroge, R.W., Tubula, M.S., Cappelli, L., Kamau, P.M., Nomade, S., Mariita, N.O., Fontijn, K., 2025. Temporal and spatial evolution of explosive silicic peralkaline eruptions at the Olkaria Volcanic Complex and Longonot volcano in the Southern Kenya Rift. Journal of Volcanology and Geothermal Research 108275. https://doi.org/10.1016/j.jvolgeores.2025.108275

Wei, W., Cai, J., Xiao, J., Meng, Q., Xiao, B., Han, Q., 2018. Kozeny-Carman constant of porous media: Insights from fractal-capillary imbibition theory. Fuel 234, 1373–1379. https://doi.org/10.1016/j.fuel.2018.08.012

Wilson, L., Sparks, R.S.J., Walker, G.P.L., 1980. Explosive volcanic eruptions — IV. The control of magma properties and conduit geometry on eruption column behaviour. Geophysical Journal of the Royal Astronomical Society 63, 117–148. https://doi.org/10.1111/j.1365-246X.1980.tb02613.x

Zhang, Y., 1999. A criterion for the fragmentation of bubbly magma based on brittle failure theory. Nature 402, 648–650.

Zhou, J.Q., Chen, Y.F., Wang, L., Cardenas, M.B., 2019. Universal Relationship Between Viscous and Inertial Permeability of Geologic Porous Media. Geophys Res Lett 46, 1441–1448. https://doi.org/10.1029/2018GL081413

Figures captions

Figure 1. a) Overview of the East African Rift, showing the location of the Rungwe Volcanic Province (RVP) along the Western Branch. Major rift faults (*red lines*) and volcanic centres (*red triangles*) are indicated.; **b)** Close-up of the main volcanic centres within the RVP, highlighting the location of the type section KF176 (*yellow star*). The red dashed contour represents the 25 cm isopach of the Rungwe Pumice deposit (modified from Fontijn et al., 2011).

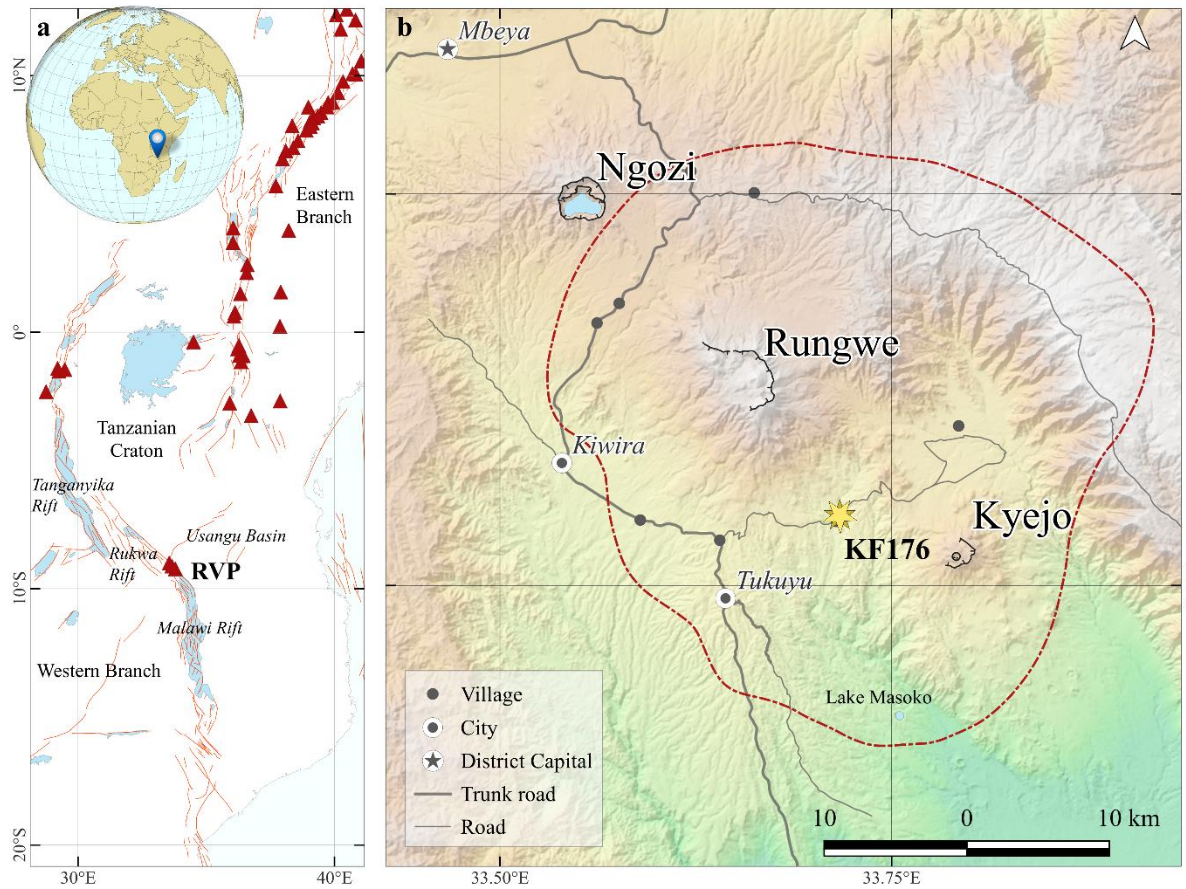

Figure 2. Image nesting method adopted for stereological conversion in FOAM, following the approach suggested by Shea (2010) over a standard RP pumiceous clast from the middle stratigraphic horizon. For each clast, two images were selected at x350 magnification, with four additional images collected at x900 magnification within these regions. Grey-scale SEM images are shown alongside their binarized, decoalesced counterparts, where white represents pumice glass and black denotes vesicles (voids). In the x75 magnified inset, also the exterior background appears black (removed during FOAM processing), and phenocrysts are displayed in grey.

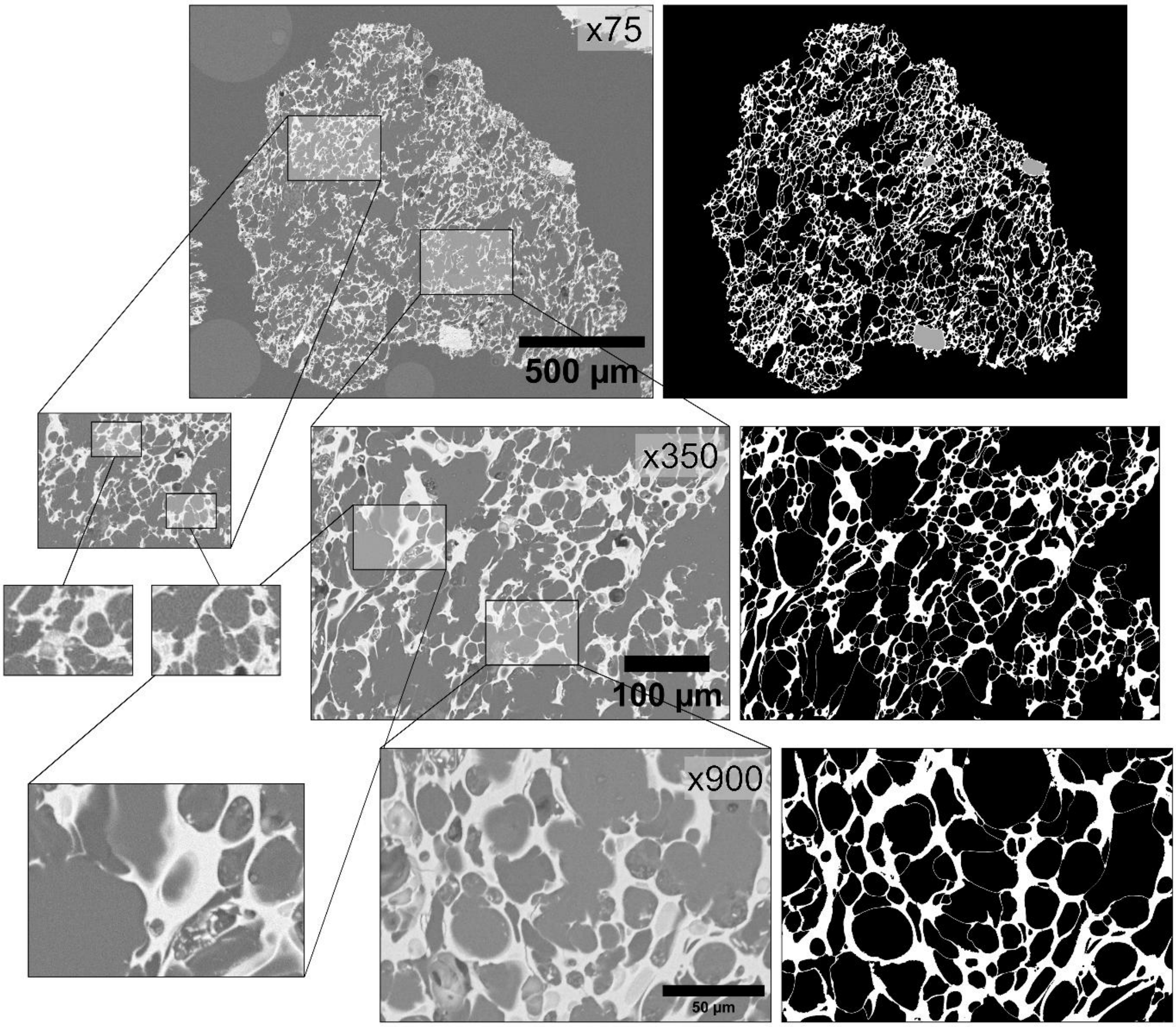

Figure 3. a) and **b)** µXCT volume reconstructions of a "standard" pumice from the middle horizon and the tube pumice, respectively, created in Dragonfly; **c)** 2D slice of a sample volume, where glass appears as light grey and vesicles as dark grey, processed through the following steps: **d)** application of the U-Net2D super-resolution model, **e)** segmentation using

the U-Net2.5D segmentation model (vesicles shown in cyan and glass in black), and **f)** vesicle separation using the watershed algorithm.

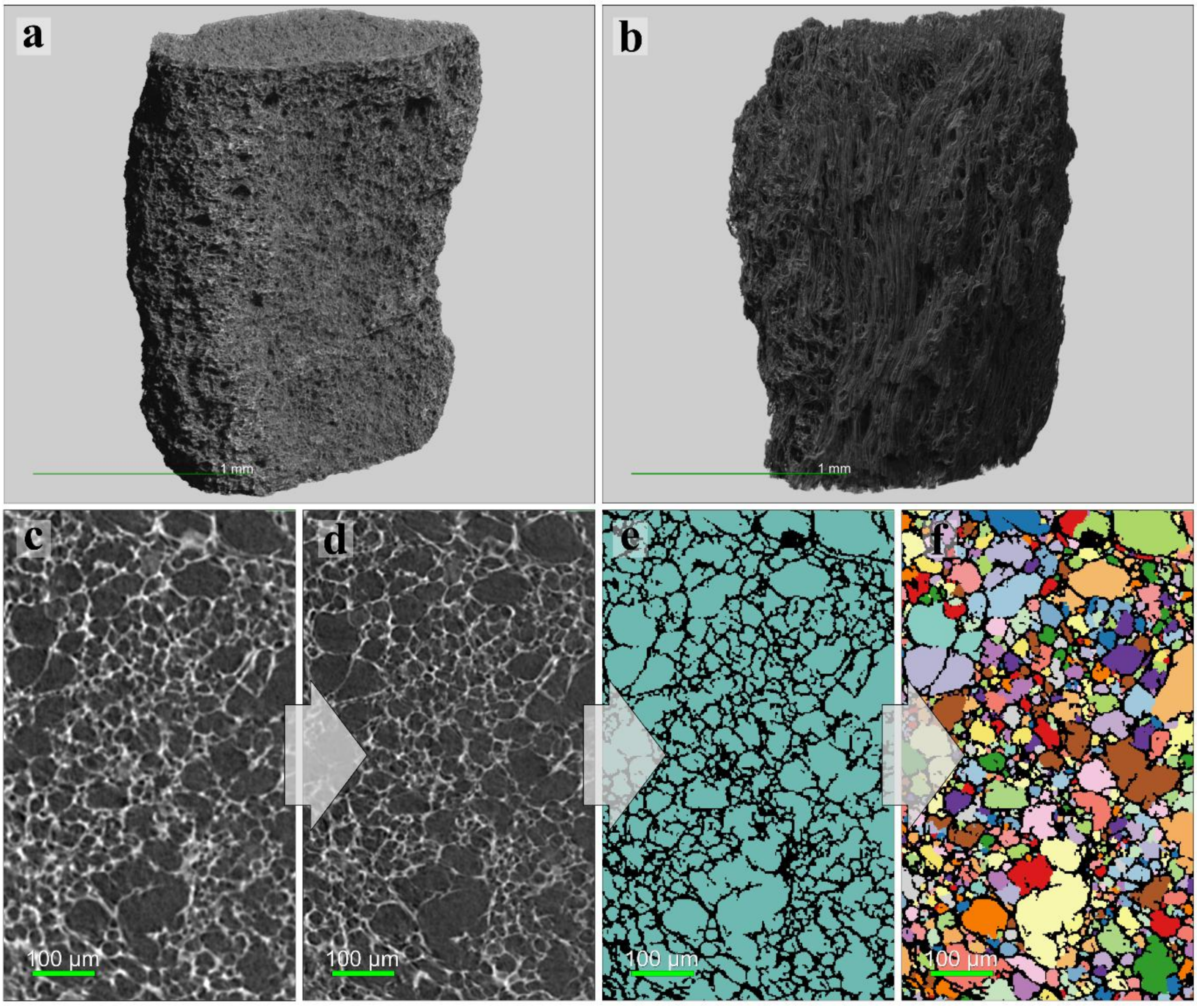

Figure 4. VVD plots for each µXCT dataset, presented individually and collectively for comparison. Most datasets exhibit lognormal, unimodal, distributions except for bottom half horizon and the tube pumice, which display a mild bimodality characterized by a secondary mode in the larger size range. This secondary mode may indicate the influence of coalescence effects on size distributions (see text for further details). The average of principal modes (red lines) corresponds to an equivalent diameter of 39 µm, with standard deviation indicated by grey dashed lines.

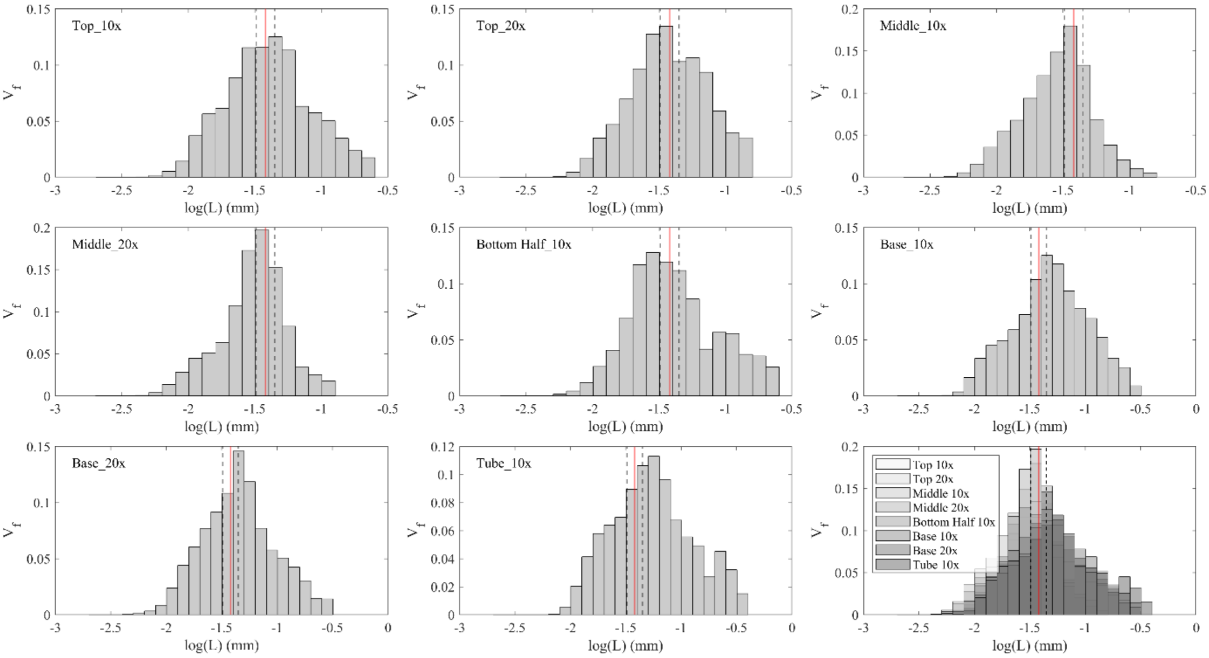

Figure 5. VSD plots for each µXCT dataset, presented individually and collectively for comparison. The slope, intercept at n_0, and goodness of fit (dashed red lines) for the linear interpolation within the smallest size range are provided for each sample.

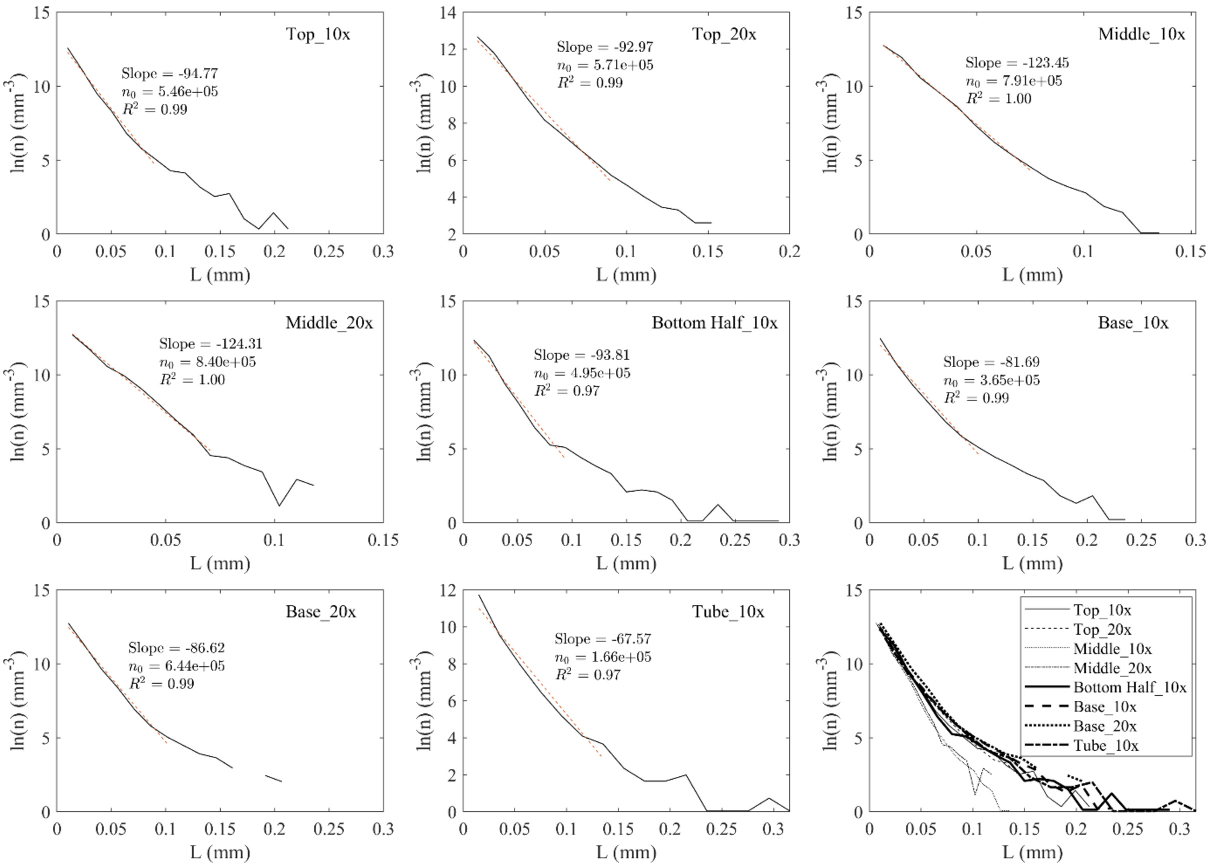

Figure 6. CVSD plots for **a)** µXCT datasets and **b)** 2D images stereologically converted with FOAM, where the µXCT trend of the base horizon is included for comparison.

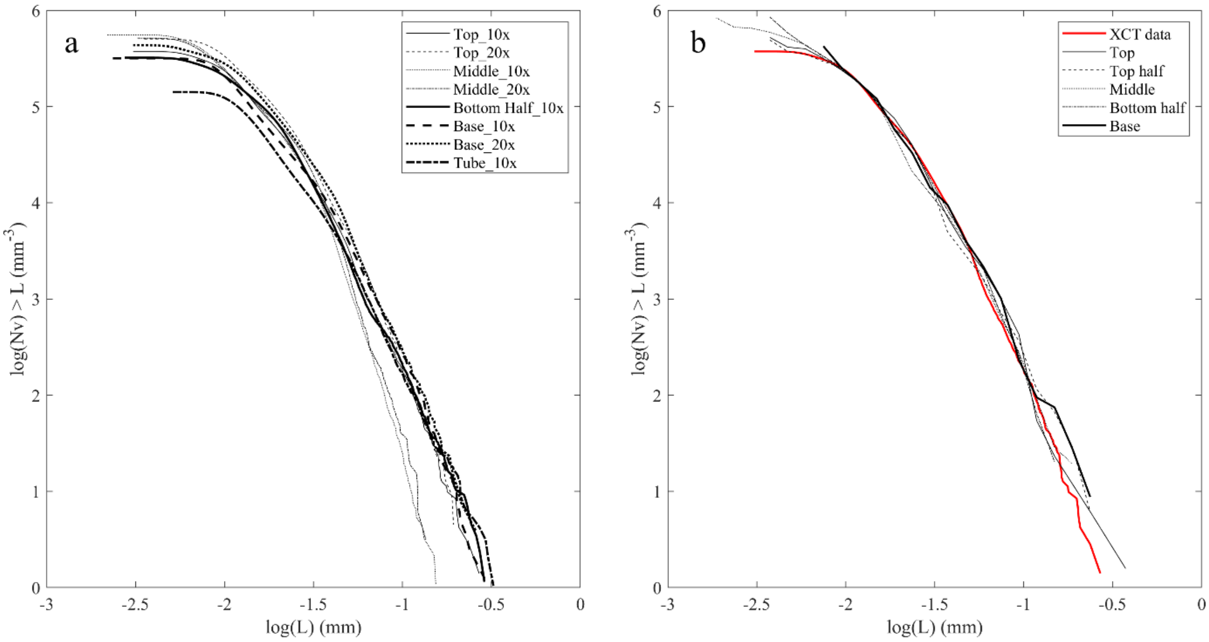

Figure 7. Box and whisker plots of decompression rates estimated by applying Shea (2017) models on 3D and 2D textural data, and the embayment diffusivity speedometer (EMBER). Whiskers indicate range limits, black horizontal lines medians, and red asterisks mean values. Previous data for explosive peralkaline magmas are included for comparison. PdB: Somma-Vesuvius Pomici di Base trachytic eruption (Pappalardo et al., 2018); PGT: Pantelleria Green Tuff trachytic eruption (Campagnola et al., 2016); 87BPR: ~87 ka Baricha peralkaline rhyolitic eruption (Tadesse et al., 2024).

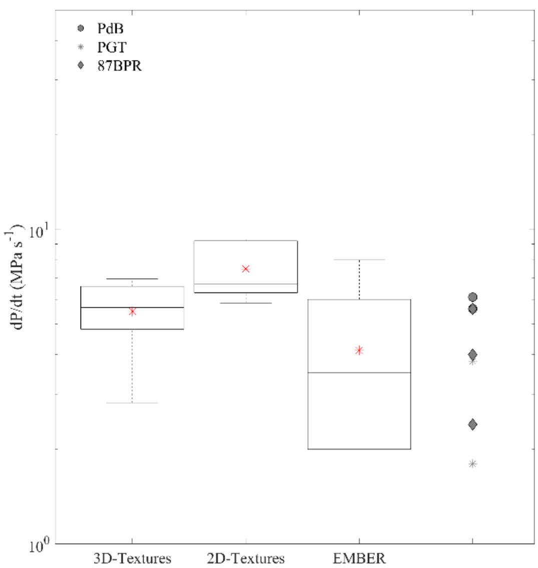

Figure 8. Stokes and Forchheimer numbers for the Rungwe Pumice (RP) samples represented as grey diamonds over a magmastatic pressure (Pm) range from 17 to 40 MPa (black arrow). The grey-shaded region represents the range for standard RP pumices, while values for the tube pumice across directions orthogonal to the main vesicle elongation are shown for comparison. Additionally, the range for the 1980 Mount St. Helens Plinian eruption (MSH1980; Degruyter et al., 2012) is indicated (dotted contour). The dashed line marks the critical Stokes and Forchheimer numbers defining the transition between effusive and explosive regimes for MSH1980 rheology (Degruyter et al., 2012); although not directly applicable to RP, a variation of maximum one order of magnitude is expected (Valdivia et al., 2022).

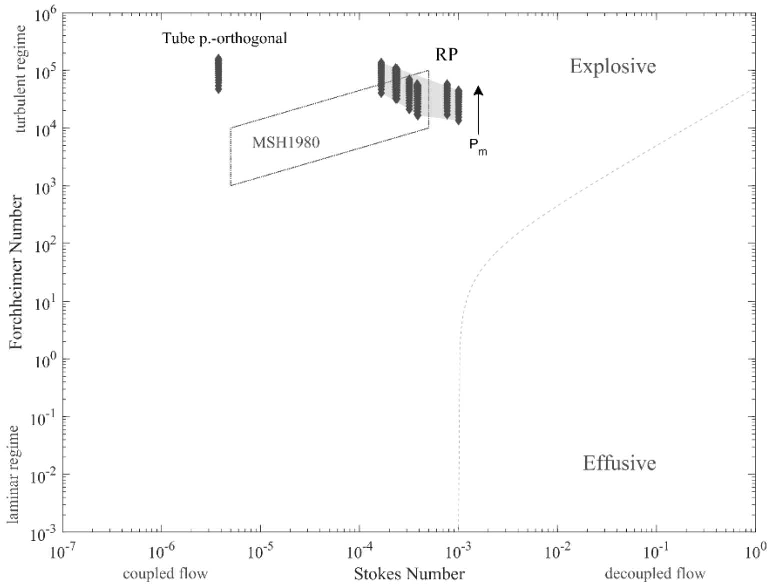

Figure 9. Comparison of key conduit parameters for different stratigraphic horizons analysed by μXCT: vesicle number density (VND), decompression rate (dP/dt), mass discharge rate (MDR), and Darcian permeability (k). An overall relative explosivity score—where 1 represents the maximum potential for explosivity—is calculated for each sample by summing the min-max normalised values of interdependent parameters promoting explosivity such as *dP/dt* and *k*. The reciprocal value of *k* was used in scoring, as it is inversely proportional to explosivity potential. Additionally, a normalised z score was calculated to express the interrelated consistency of these parameters.

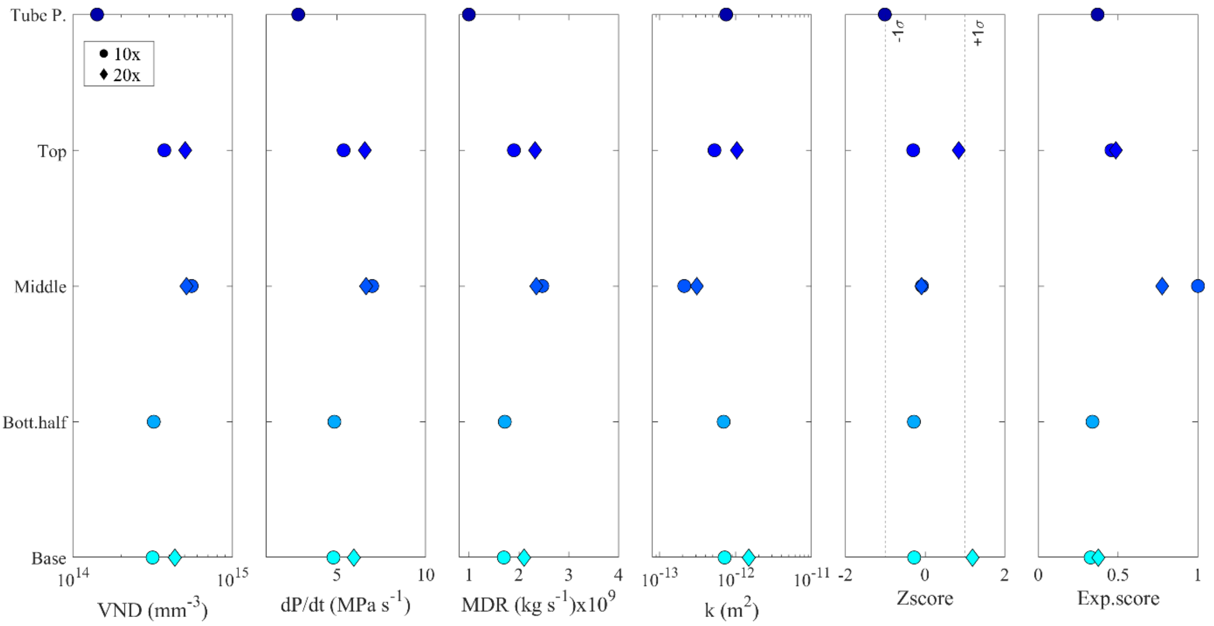

Figure 10. Grey-scale three-dimensional reconstructions and segmented vesicle volumes of a **a)** "standard" pumice and the **b)** tube pumice, providing a visual comparison of vesicle textures. In **b)** the y-axis indicates the direction of vesicle preferential orientation. Both particles were scanned with a 10x magnification lens.

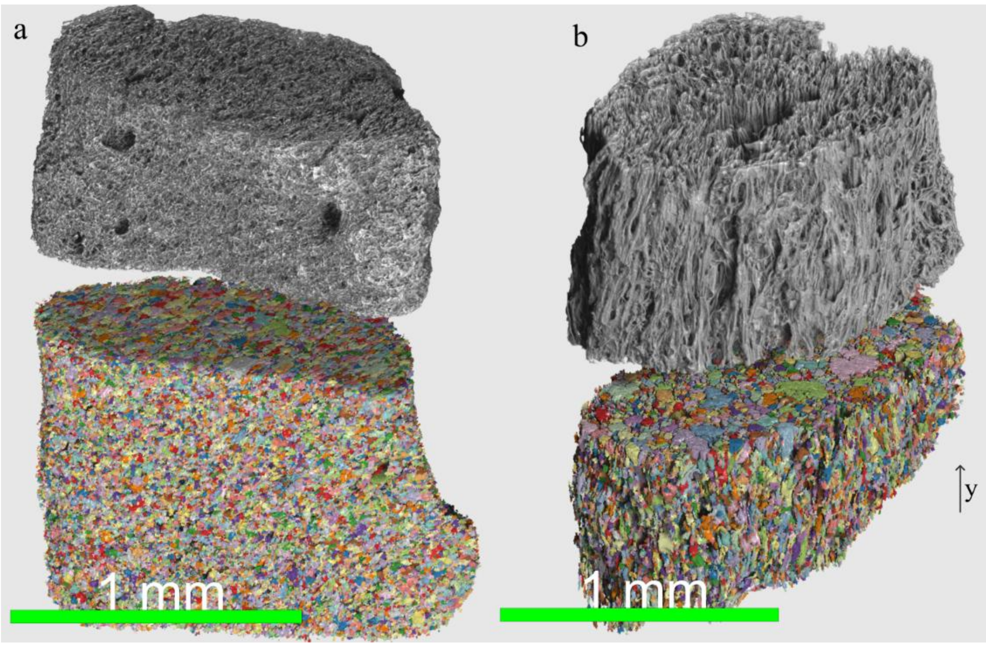

Figure 11. Different fragmentation criteria applied to the melt compositions of melt embayments spanning their water concentration range—from innermost (H_2O_{int}; thickest line) to outmost (H_2O_{out}; thinnest line) portions. The minimum water concentration inferred for a quenching pressure of 17 MPa (black dashed line) is also shown. The criteria have been evaluated for a range of temperatures (700-1000 °C) to represent the temperature drop due to

the gas expansion upon ascent (see text for further details). Only one sample from the middle horizon is shown for clarity. **a)** Strain rate criterion is represented by melt structural relaxation drops caused by viscosity increase due to magma degassing and cooling. The grey inset highlights the close-up in the low-temperature region shown in **b)**, where the criterion is satisfied when the critical strain rate (0.08 s^{-1}) exceeds the structural relaxation time. The hypothetical strain rate (3.90 s^{-1}) resulting from magma acceleration only within the last ~55 m of ascent is also shown; **c)** shear-induced fragmentation criterion expressed as viscosity increase, where fragmentation is expected when the viscosity exceeds the critical viscosity calculated for RP conditions (μ_{crit}). Average of μ_{crit} for all samples is indicated with a red line together with $\pm 1\sigma$ (grey dashed lines); **d)** increase in bubble internal gas overpressure with increasing melt viscosity upon ascent where fragmentation is expected when the overpressure exceeds the average critical value of 3.54 MPa (red line with $\pm 1\sigma$ indicated by grey dashed lines).

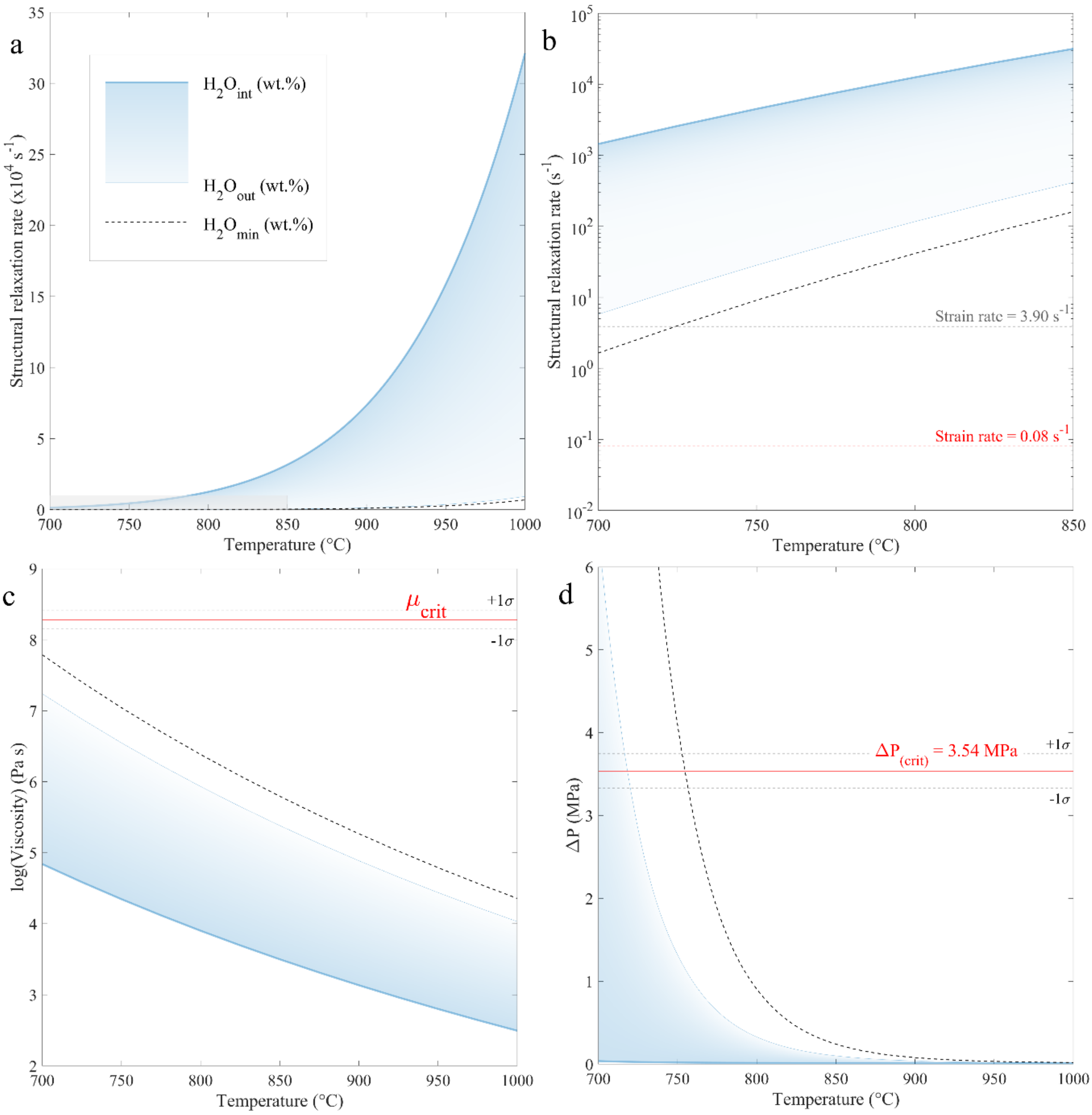
a
H_2O_{int} (wt.%)
H_2O_{out} (wt.%)
H_2O_{min} (wt.%)
Structural relaxation rate (x10^4 s^{-1})
Temperature (°C)
b
Strain rate = 3.90 s^{-1}
Strain rate = 0.08 s^{-1}
Structural relaxation rate (s^{-1})
Temperature (°C)
c
μ_{crit}
+1σ
-1σ
log(Viscosity) (Pa s)
Temperature (°C)
d
$\Delta P_{(crit)}$ = 3.54 MPa
+1σ
-1σ
ΔP (MPa)
Temperature (°C)

Tables

Table 1. Vesicularity, VND, and geometric parameters of pumice textures analysed with 2D and 3D methods.

Sample	3D Textures							2D Textures†		FOAM†
	Lens	Envelope volume⸸ (mm³)	Vesicle number	VND (m^{-3})	Vesicularity	Connectivity	Surface Area per unit volume (mm^{-1})	Vesicularity *	VND** (m^{-3})	VND (m^{-3})
Top	10X	1.884	2.65×10^{5}	3.73×10^{14}	0.62	0.9986	145	0.76 ±0.05	$4.06 \pm 2.10 \times 10^{14}$	5.23×10^{14}
	20X	0.749	1.11×10^{5}	5.04×10^{14}	0.71	0.9999	160			
Top half								0.77 ±0.04	$4.92 \pm 3.60 \times 10^{14}$	4.91×10^{14}
Middle	10X	2.089	5.13×10^{5}	5.53×10^{14}	0.56	0.9993	182	0.72 ±0.08	$2.38 \pm 1.55 \times 10^{14}$	8.34×10^{14}
	20X	0.791	1.65×10^{5}	5.14×10^{14}	0.59	0.9997	188			
Bottom half	10X	2.312	2.79×10^{5}	3.21×10^{14}	0.62	0.9996	150	0.76 ±0.04	$3.61 \pm 2.38 \times 10^{14}$	8.53×10^{14}
Base	10X	2.227	2.54×10^{5}	3.15×10^{14}	0.64	0.9998	158	0.71 ±0.05	$3.84 \pm 3.00 \times 10^{14}$	4.24×10^{14}
	20X	0.914	1.14×10^{5}	4.35×10^{14}	0.71	0.9999	151			
Tube pumice	10X	2.155	1.36×10^{5}	1.42×10^{14}	0.56	0.9985	129			
Average‡				$4.31 \pm 8.95 \times 10^{14}$	0.64 ±0.05	0.9995 ±0.0004	162 ±15	0.74 ±0.06	$3.76 \pm 2.75 \times 10^{14}$	$6.25 \pm 1.81 \times 10^{14}$

⸸Volume of glass+vesicles. Open vesicles with an outlet diameter ≤70µm were closed by a wrapping surface; ‡ average of parameters for 3D datasets is calculated considering only "standard" pumices; † for each horizon, 2D Vesicularity and VND are given by the average of processed images for 10 different samples; *2D vesicularity is computed as fraction of vesicle area (excluding vesicles at borders) over total area (corrected for border vesicles); **2D VND is estimated from number per the unit area: Na/L where L is the average vesicle dimension, which can be written as Na/√(A/n) with A: total vesicle area and n: number of vesicles; †2D VND stereologically corrected using FOAM.

Table 2. Indicators derived from 3D size distribution trends and shape parameters. The slope and intercept of VSDs are provided, along with the estimated average growth rate.

Sample	Lens	VSD Slope (mm^{-1})	VSD n_0 (mm^{-3})	Average bubble growth rate ($mm \cdot s^{-1}$)	VVD equivalent diameter mode (μm)	Average sphericity
Top	10X	-95	5.46×10^5	6.64×10^{-4}	45	0.74 ±0.09
	20X	-93	5.71×10^5	8.27×10^{-4}	36	0.70 ±0.09
Middle	10X	-123	7.91×10^5	6.59×10^{-4}	36	0.74 ±0.10
	20X	-124	8.40×10^5	6.26×10^{-4}	36	0.70 ±0.10
Bottom half	10X	-94	4.95×10^5	6.06×10^{-4}	28	0.73 ±0.10
Base	10X	-82	3.65×10^5	6.88×10^{-4}	45	0.71 ±0.10
	20X	-87	6.44×10^5	8.04×10^{-4}	45	0.71 ±0.10
Tube pumice	10X	-68	1.66×10^5	4.93×10^{-4}	57	0.68 ±0.12
Average				$6.71 \pm 1.00 \times 10^{-4}$	39 ±6*	

*Average VVD mode is calculated considering only "standard" pumices.

Table3. Estimates of decompression rate calculated using both Shea (2017) equation for pumice textures and the embayment speedometer for comparison. Estimated supersaturation pressure (ΔP_{sat}), nucleation pressure (P_n), mass discharge rate (MDR), and outgassing parameters are also reported.

Sample	Lens	3D Textures: Decompression rate ($MPa\cdot s^{-1}$)	Ascent rate ($m\cdot s^{-1}$)	ΔP_{sat} (MPa)	P_n (MPa)	MDR $\times10^9$ ($kg\cdot s^{-1}$)	2D Textures†: Decompression rate ($MPa\cdot s^{-1}$)	Emb. Speedometer: Sample	Decompression rate ($MPa\cdot s^{-1}$)
Top	10X	5.4	199	52	40	1.90×10^9	6.7	Top	8.0
	20X	6.6	243	52	40	2.32×10^9		Top	8.0
Top half							6.5	Top	2.0
Middle	10X	7.0	259	52	40	2.47×10^9	9.2	Top half	4.0
	20X	6.6	246	52	40	2.35×10^9		Top half	4.0
Bottom half	10X	4.9	180	52	40	1.71×10^9	9.3	Top half	3.0
								Top half	2.0
Base	10X	4.8	178	52	40	1.70×10^9	5.9	Middle	2.0
	20X	5.9	220	52	40	2.10×10^9		Bottom half	9.0
Tube pumice	10X	2.8	104	52	40	9.94×10^8			
Average‡		5.9 ±0.9	45 ±7	52	40	2.08×10^9 $\pm0.6\times10^8$	7.5 ±1.5		4.7 ±2.7

Outgassing parameters*

Sample	Lens	Darcian permeability (m^2) x	Darcian y	Darcian z	Inertial permeability (m^2) x	Inertial y	Inertial z	Stockes number x	Stockes y	Stockes z
Top	10X	4.84×10^{-13}	4.36×10^{-13}	6.56×10^{-13}	3.26×10^{-9}	2.83×10^{-9}	4.91×10^{-9}	3.46×10^{-5}	3.12×10^{-5}	4.68×10^{-5}
	20X	1.09×10^{-12}	8.77×10^{-13}	1.14×10^{-12}	9.76×10^{-9}	7.28×10^{-9}	1.04×10^{-8}	6.42×10^{-5}	5.17×10^{-5}	6.74×10^{-5}
Middle	10X	3.45×10^{-13}	1.27×10^{-13}	1.60×10^{-13}	2.06×10^{-9}	5.34×10^{-10}	7.28×10^{-10}	2.86×10^{-5}	1.05×10^{-5}	1.33×10^{-5}
	20X	2.53×10^{-13}	2.14×10^{-13}	4.55×10^{-13}	1.35×10^{-9}	1.08×10^{-9}	3.00×10^{-9}	2.13×10^{-5}	1.80×10^{-5}	3.83×10^{-5}
Bottom half	10X	6.35×10^{-13}	7.90×10^{-13}	6.57×10^{-13}	4.71×10^{-9}	6.32×10^{-9}	4.92×10^{-9}	4.10×10^{-5}	5.10×10^{-5}	4.24×10^{-5}
Base	10X	7.73×10^{-13}	6.41×10^{-13}	7.30×10^{-13}	6.13×10^{-9}	4.76×10^{-9}	5.68×10^{-9}	5.05×10^{-5}	4.19×10^{-5}	2.53×10^{-5}
	20X	1.57×10^{-12}	1.47×10^{-12}	1.42×10^{-12}	1.60×10^{-8}	1.46×10^{-8}	1.40×10^{-8}	1.42×10^{-4}	1.33×10^{-4}	1.29×10^{-4}
Tube pumice	10X	1.18×10^{-14}	7.49×10^{-13}	5.15×10^{-14}	2.15×10^{-11}	5.87×10^{-9}	1.57×10^{-10}	3.95×10^{-7}	2.50×10^{-5}	1.72×10^{-6}

‡Average of 3D datasets is calculated considering only "standard" pumices; † obtained from VND values corrected with stereological conversion in FOAM; *parameters estimated across three mutually orthogonal and randomly oriented directions.

Supplementary Information

List of Supplementary Material accompanying the manuscript:

a- **Table SM1:** Major element composition of glass embayments, melt inclusion references, and standards analysed with SEM-EDX. Water concentrations measured using Raman spectroscopy across melt embayment transects are also included (available upon request to lorenzo.cappelli@ulb.be).

b- 3D volume reconstructions in Dragonfly.

c- Integration of vesicle size distribution plots

d- Shape parameters

e- Pumice lapilli vesicularity

Stratigraphic samples chose as representative for each horizon during 2D and 3D textural investigations:

Stratigraphic horizon	Sample
Top	KF176 O
Top half	KF176 L
Middle	KF176 I
Bottom half	KF176 F
Base	KF176 C
Tube pumice	KF176 L

(NB: KF176L refers to top half horizon in 2D dataset, while it refers to tube pumice in 3D dataset).

b. 3D volume reconstructions in Dragonfly for samples not showed in Figure 2 of the main text. Only samples acquired with 10x lens are presented to show whole clasts morphologies.

Figure SM1: 3D reconstruction of base horizon (KF176 C).

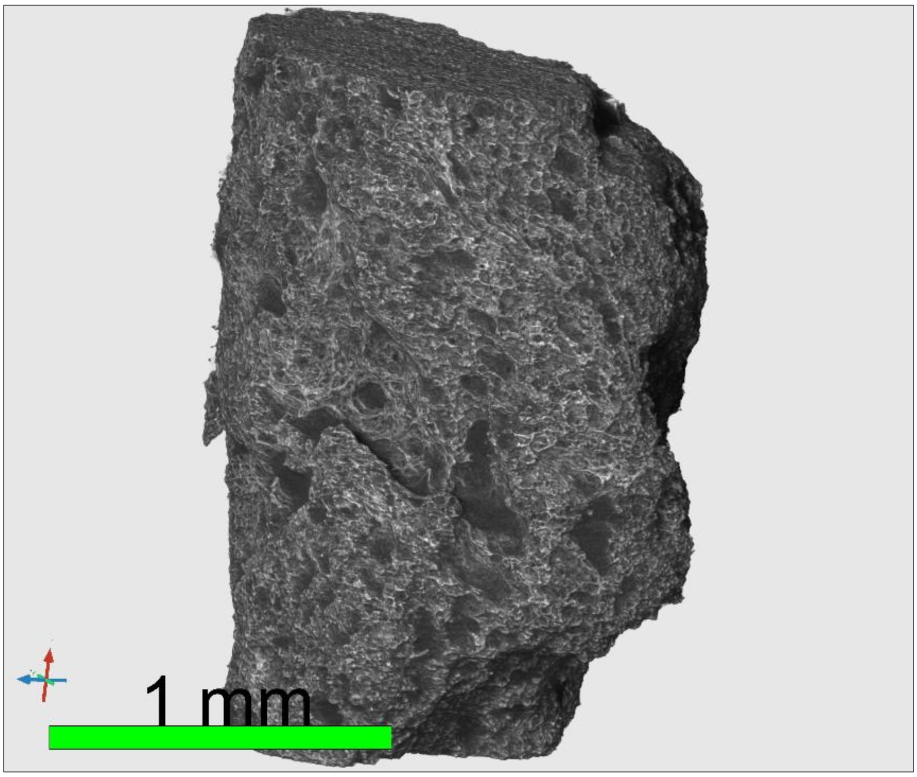

Figure SM2: 3D reconstruction of bottom half horizon (KF176 F).

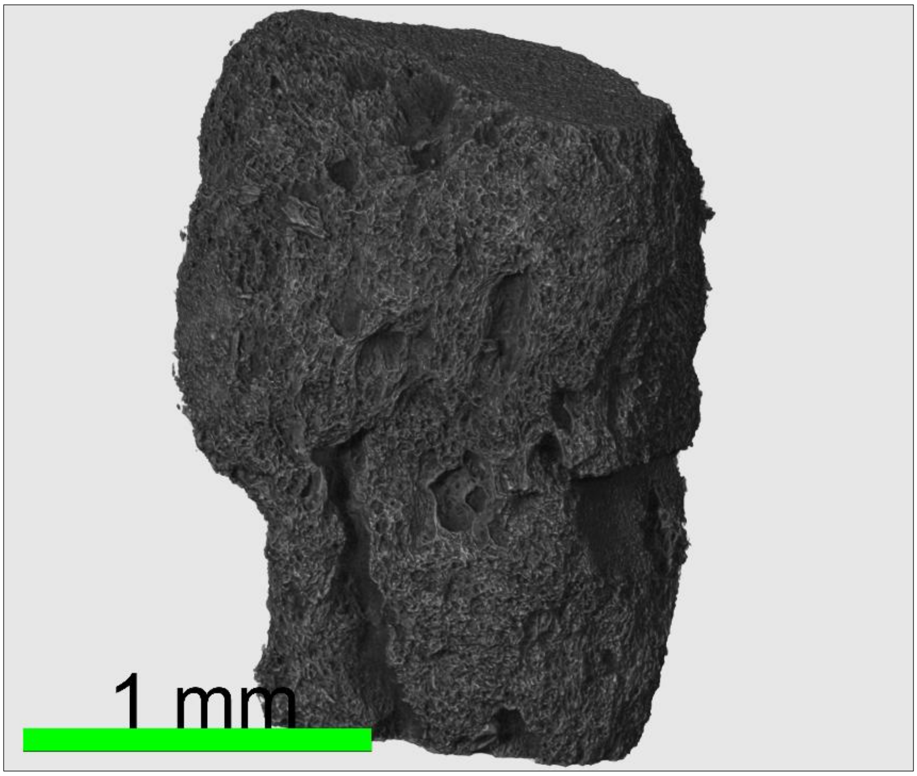

Figure SM3: 3D reconstruction of top horizon (KF176 O).

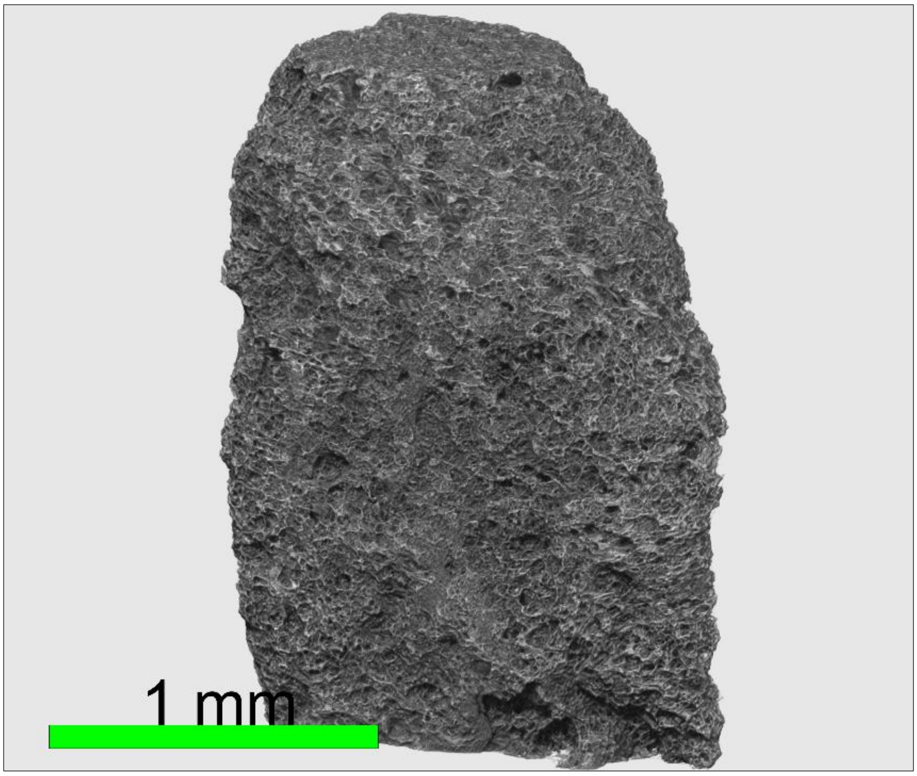

c. Integration of vesicle size distribution plots

Figure SM4: Vesicle size distributions for 2D datasets processed with FOAM. Trends are consistent with continuous nucleation and growth of bubbles, resulting in a curve that is badly interpolated by straight lines, especially toward the large size range. However, linear fitting has been attempted in correspondence with slope breaks. Slope and intercept at L=0 mm for each trend are reported in the figure. (Sample KF176L refers to top half horizon).

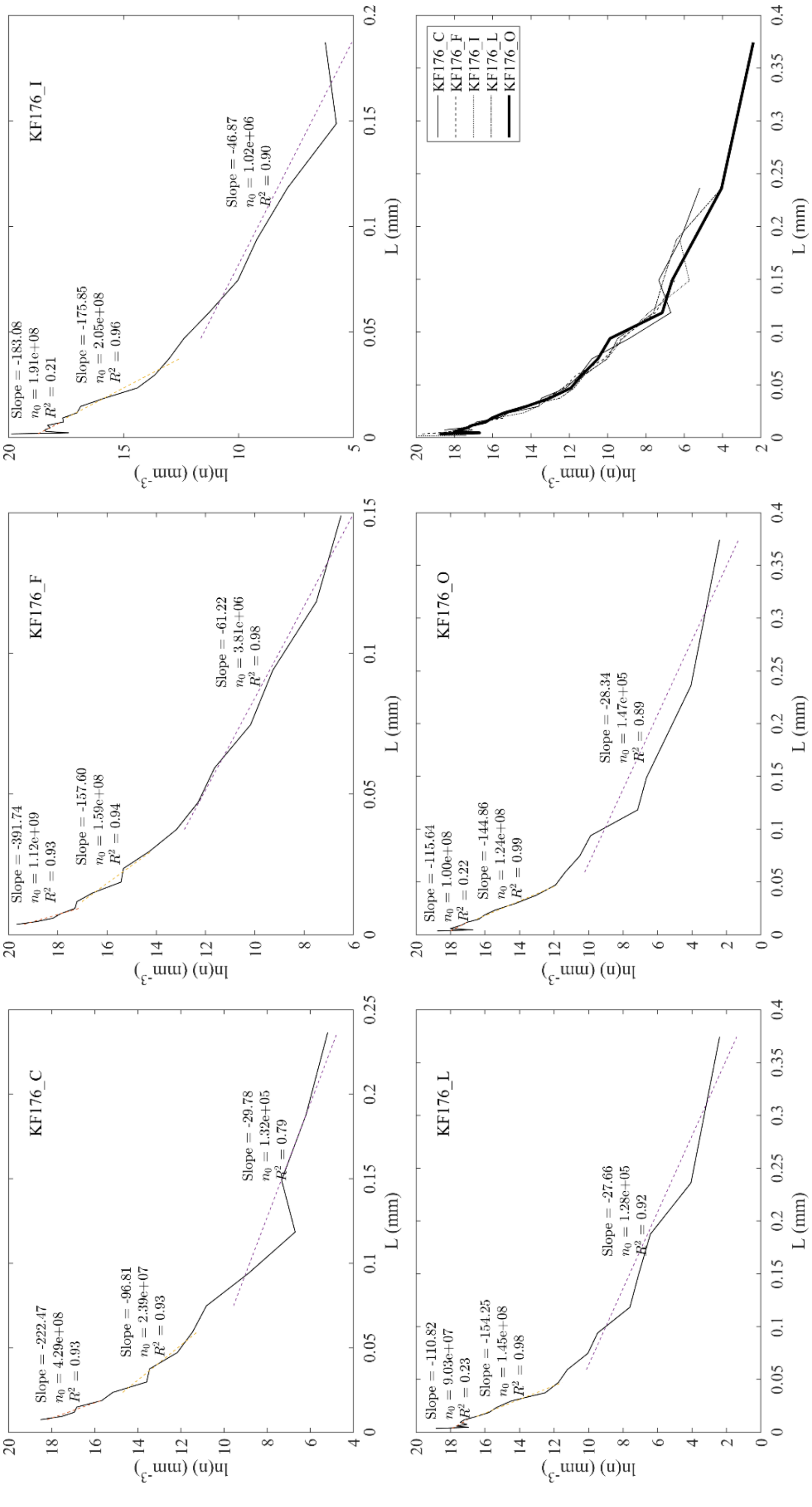

Figure SM5: Cumulative vesicle size distribution (CVSD) trends of 2D texture samples processed with FOAM. The distributions are fitted to an exponential trend, with the coefficients reported in the figure. Additionally, an attempt to fit two power-laws in correspondence with slope breakings is shown with their respective exponents also indicated in the figure. (Sample KF176L refers to top half horizon).

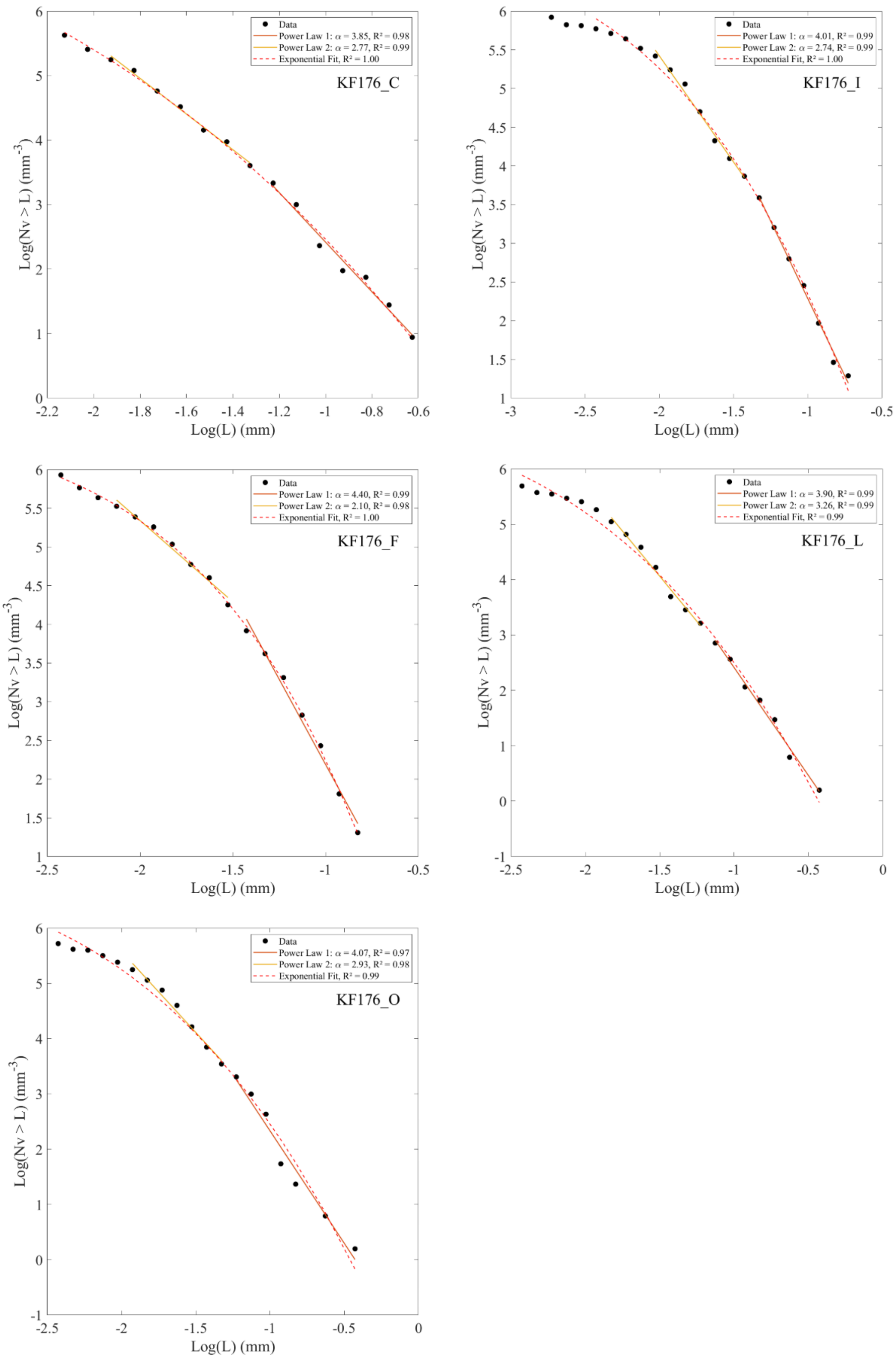

Table SM2: Exponents and goodness of fitting for first and second power law fit of CVSDs (Figure SM5), together with the coefficients for exponential interpolation.

Sample	NumSegments	Slope_2	Slope_3	n_0_2	n_0_3	R^2_2	R^2_3	VVD modes (μm)
Top	2	-144.86	-28.34	1.24E+08	1.47E+05	0.99	0.89	94
Top half	2	-154.25	-27.66	1.45E+08	1.28E+05	0.98	0.92	30
Middle	2	-175.85	-46.87	2.05E+08	1.02E+06	0.96	0.90	94
Bottom half	2	-157.60	-61.22	1.59E+08	3.81E+06	0.94	0.98	24
Base	2	-96.81	-29.78	2.39E+07	1.32E+05	0.93	0.79	37

Stratigraphic horizon	Sample
Top	KF176 O
Top half	KF176 L
Middle	KF176 I
Bottom half	KF176 F
Base	KF176 C
Tube pumice	KF176 L

Figure SM6: CVSD trends of µXCT samples. The distributions are fitted to an exponential trend, with the coefficients reported in the figure. Additionally, an attempt to fit two power-laws in correspondence with slope breakings is shown with their respective exponents also indicated in the figure. (Sample KF176L refers to tube pumice)**.**

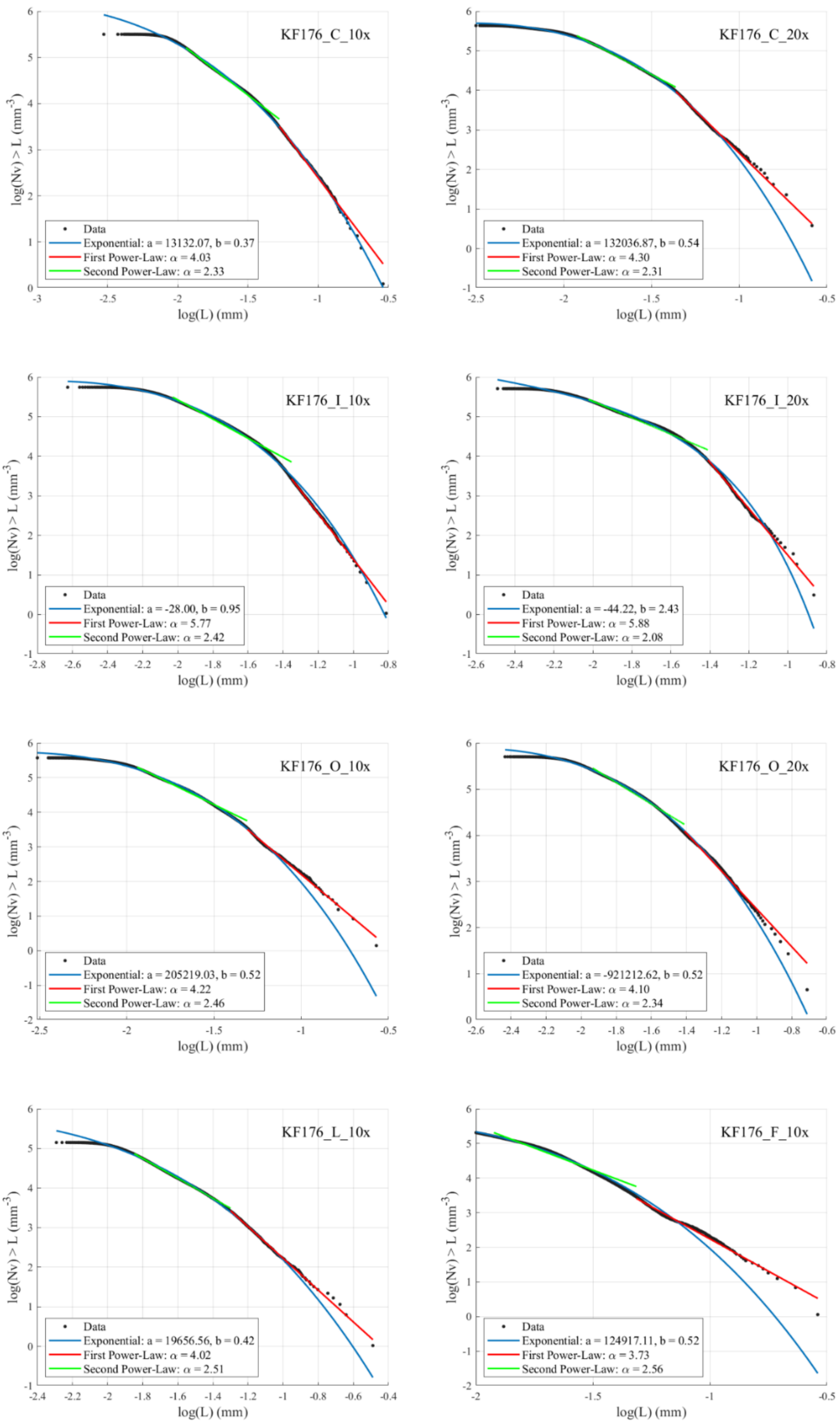

d. Shape parameters

Figure SM7: a) Elongation and **b)** regularity of vesicles from 2D texture datasets processed with FOAM. The shape parameter distributions reveal a tendency toward minimal elongation (indicative of equivalent bounding ellipsoid axes) and high perimeter regularity, suggesting a preference for subcircular vesicle shapes. (Sample KF176L refers to top half horizon)**.**

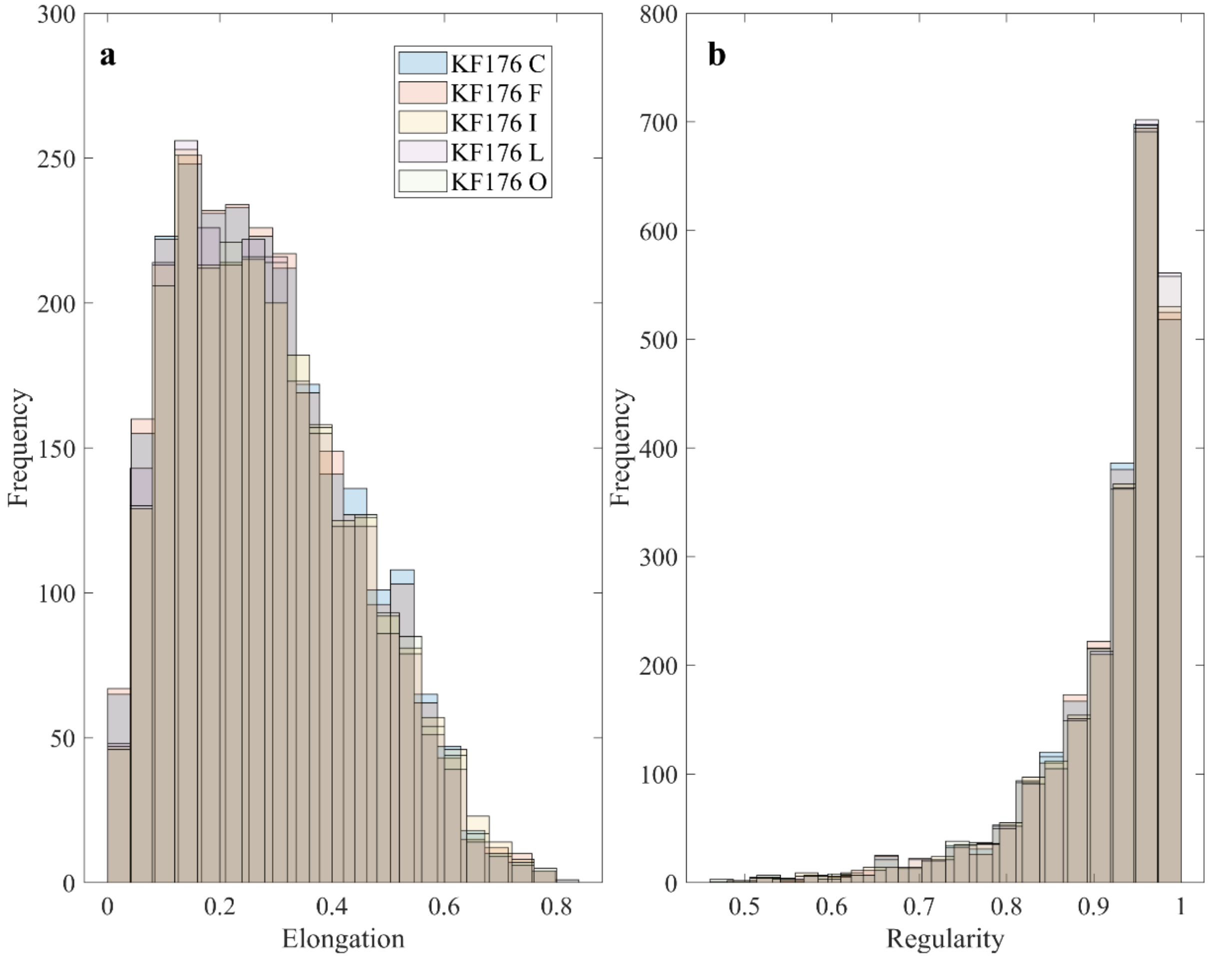

Figure SM8: Frequency distribution of 3D sphericity and its relationship with vesicle size (equivalent diameter L) for XCT samples. Only samples KF176I-10x (middle horizon) and KF176L-10x (tube pumice) are shown for comparison. Sphericity values confirm the tendency toward circular perimeters observed in 2D sections (Figure SM7), supporting the validity of assuming spherical volumes for stereological conversion in FOAM.

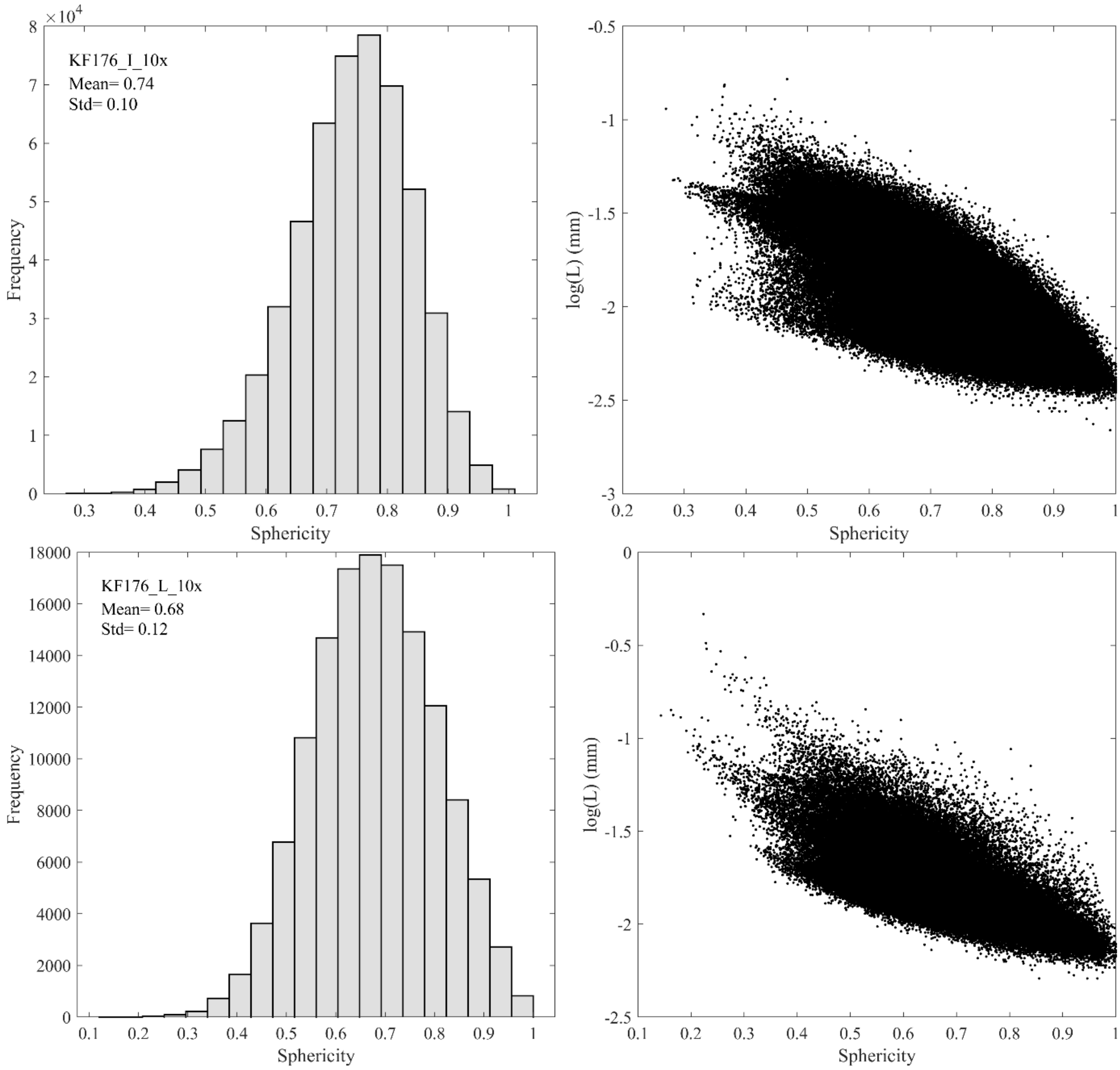

Figure SM9: Preferential orientation of vesicles measured as the orientation of the major axis of vesicle bounding ellipsoids relative to a randomly oriented Cartesian coordinate system, with the z-axis corresponding to the sample rotational axis during μXCT data acquisition. Orientations are expressed as orientation density (number of vesicles with equivalent orientation per sample volume). Notably, the tube pumice (KF176L) exhibits the maximum iso-orientation, while bottom half (KF176F) and middle (KF176I) also show concentrated vesicle orientation. This suggests that, despite vesicles being predominantly subspherical, shear forces were sufficient to direct bubble orientation, even in more internal portions of the conduit far from conduit walls. Pixels of pole figures have a dimension of 1x1 deg.

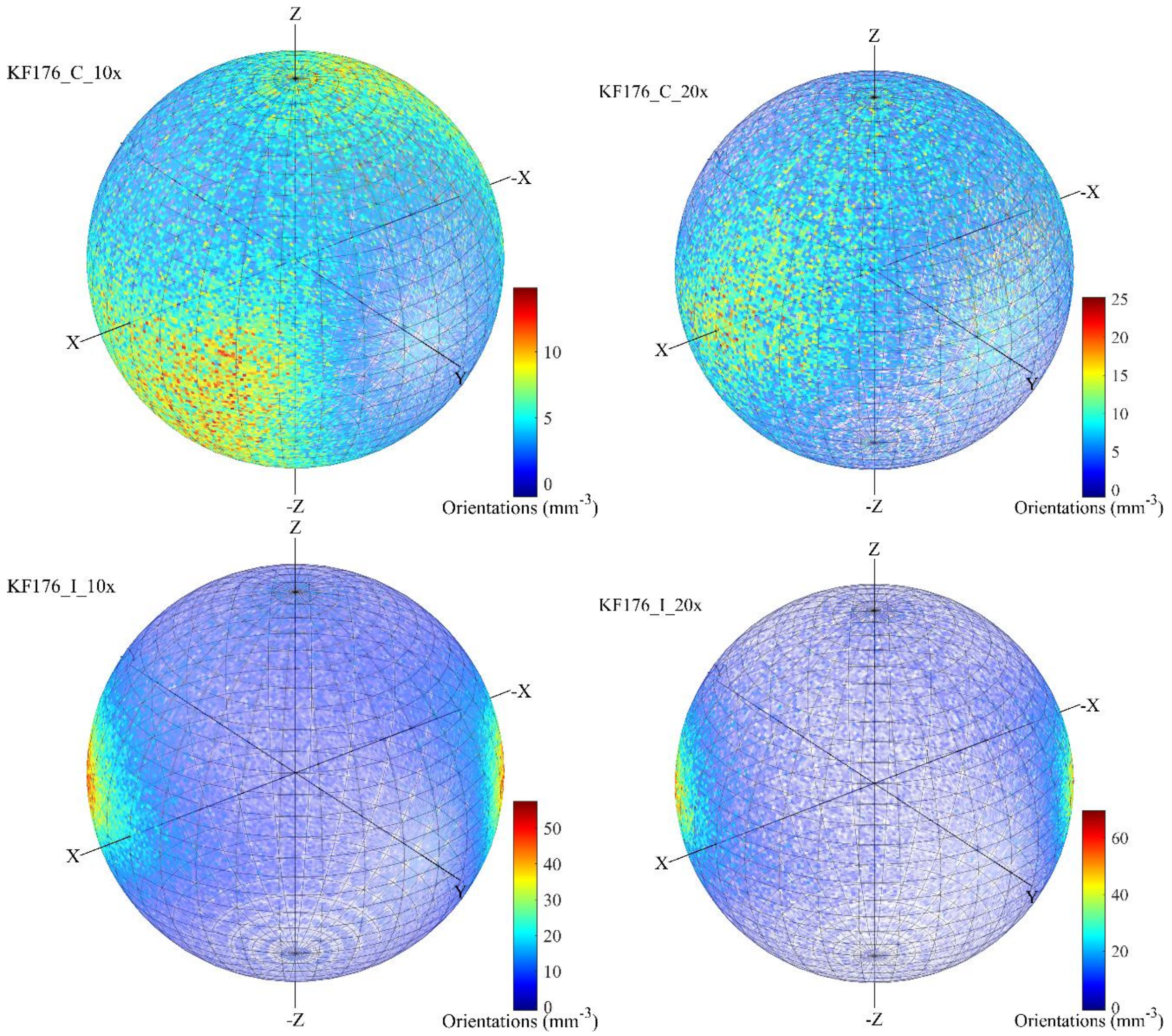

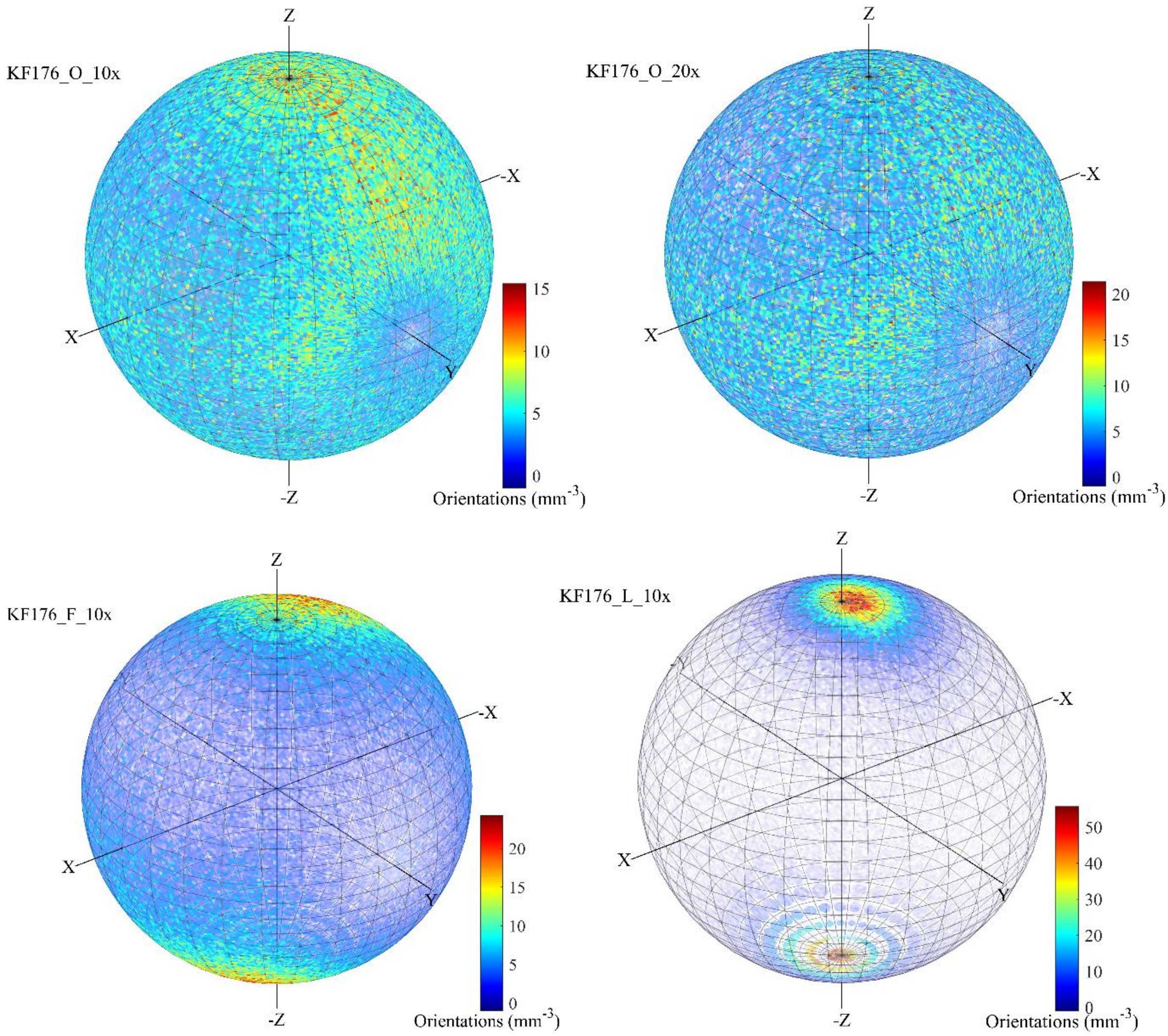
KF176_O_10x
KF176_O_20x
KF176_F_10x
KF176_L_10x
Z
-Z
X
-X
Y
Orientations (mm^{-3})
0
5
10
15
20
30
40
50

e. Pumice lapilli vesicularity

e.1. *Method*

The density of pumice clasts was measured using all available clasts within the -4/-5 φ (16-32 mm) grain size range from all stratigraphic horizons in each subsample. Depending on clast abundance, between 40 and 75 clasts were collected per horizon for a total of ~300 samples. Clasts were then rinsed with multiple cycles of ultrasonic bath to remove adhering fine dust.

A Micromeritics AccuPyc II 1345 gas (helium) displacement pycnometer was used at the Université libre de Bruxelles (Belgium) to measure the bulk volume (i.e., rock skeleton plus closed vesicles) of clasts. Each clast's volume was measured ten times and the values averaged ($\pm 1\sigma_{Max} = 0.092$ g cm^{-3}). Then, the bulk density was obtained by dividing the measured volumes by clast mass, determined with a high-precision scale (0.0001 g resolution). For the same clasts, the envelope density (i.e., rock skeleton plus open and closed vesicles) was measured with a VWR® Balance equipped with a VWR® Density Kit based on Archimedes' principle. To seal open vesicles, samples were wrapped in a thin plastic film. The density was calculated from the difference between the sample mass in air and its mass when submerged in distilled water. Measured densities were then corrected for the mass and volume of the plastic wrap. Results were additionally validated on a small subset of samples using a Micromeritics GeoPyc pycnometer (at the Université libre de Bruxelles, Belgium) which determines envelope volume—and thus density—by measuring the displacement of a quasi-fluid medium composed of rigid microscopic beads (i.e., Dry Flo™ compound). Finally, true glass density (i.e., dense rock equivalent, representing the pumice skeleton) was determined for each stratigraphic horizon using the gas pycnometer with finely crushed pumice powders (≤ 63 μm), that were devoid of major vesicularities.

Eventually, bulk (ρ_{Blk}), envelope (ρ_{Env}), and true (ρ_{DRE}) densities were used to calculate the open (φ_{Opn}), closed (φ_{Clos}), and total (φ_{Tot}) vesicularity of clasts:

$$\varphi_{\mathrm{Opn}} = \frac{(\rho_{\mathrm{Blk}} - \rho_{\mathrm{Env}})}{\rho_{\mathrm{Blk}}} \qquad (a1)$$

$$\varphi_{\mathrm{Tot}} = \frac{(\rho_{\mathrm{DRE}} - \rho_{\mathrm{Env}})}{\rho_{\mathrm{DRE}}} \qquad (a2)$$

$$\varphi_{\mathrm{Clos}} = \rho_{\mathrm{Tot}} - \rho_{\mathrm{Opn}} \qquad (a3)$$

a.2. *Results*

The average total vesicularity of pumice lapilli was measured at ~85% ±4%, with no visible change across different stratigraphic horizon (**Fig**. **SM11**). Within the same horizon, clasts show similar values, with a maximum standard deviation (±1σ) of ±5%. Open vesicularity corresponds to total vesicularity, as closed vesicularity is recorded to be always around 0%, indicating fully connected vesicle networks (**Fig. SM11**).

Table SM3: Densities and vesicularities for pumice lapilli clasts, presented as averages for each horizon.

Stratigraphic subsample	Particle Count	Glass density (g/cm^3)	Bulk density (g/cm^3)	Envelope density (g/cm^3)	Total Vesicularity (%)	Open Vesicularity (%)	Closed Vesicularity (%)
Top	61	2.34 (±0.00)	2.49 (±0.12)	0.36 (±0.07)	85.0 (±3.1)	85.5 (±3.3)	-0.5 (±0.6)
Top half	46	2.36 (±0.02)	2.47 (±0.13)	0.38 (±0.08)	84.1 (±3.4)	84.5 (±3.6)	-0.4 (±0.7)
Middle	75	2.38 (±0.01)	2.43 (±0.10)	0.37 (±0.09)	84.4 (±3.7)	84.6 (±3.9)	-0.2 (±0.6)
Bottom half	73	2.39 (±0.01)	2.47 (±0.13)	0.35 (±0.13)	85.3 (±5.5)	85.6 (±5.8)	-0.3 (±0.7)
Base	31	2.39 (±0.01)	2.64 (±0.13)	0.31 (±0.08)	86.9 (±3.3)	88.1 (±3.5)	-1.2 (±0.5)
Total	**286**	**2.37 (±0.02)**	**2.50 (±0.13)**	**0.35 (±0.10)**	**85.1 (±4.1)**	**85.7 (±4.4)**	**-0.5 (±0.7)**

Figure SM10: (left) Box and whisker plots of pumice lapilli vesicularity for the different horizon of the KF176 deposit, and their (right) connected vesicularity.

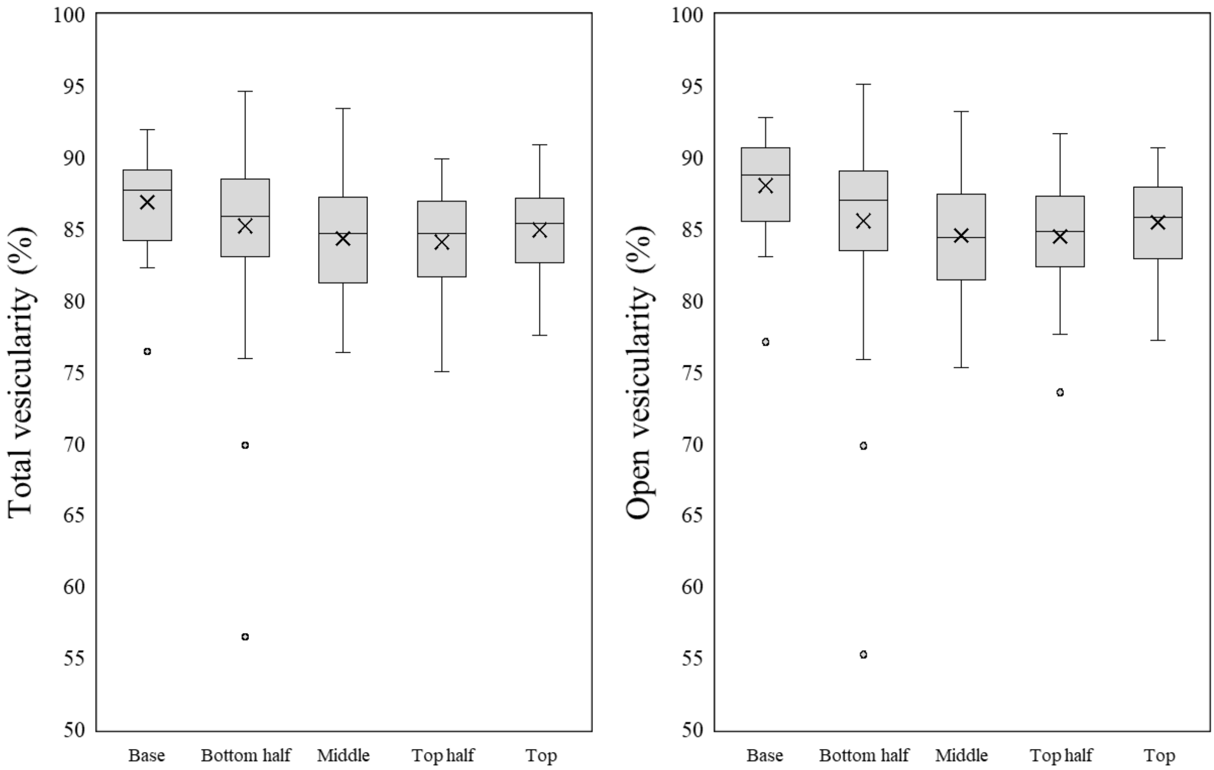

Figure SM11: Mosaic of SEM images of a thin section of a lapilli-sized pumiceous clast from sample KF176N. Notably inflated bubbles at the core of the clast reach up to millimetric size. Accurate textural investigations on these clasts resulted impractical due to preparation-produced artefacts and to polishing materials and pumiceous fine dust accumulated in voids.